PUTTING QUANTUM INTO MECHANICS

Theoretical Investigation of Nano-Electro-Mechanical Systems

CMTH-MacKinnon-2

CID:00731717, April 2017

Supervisor: Prof. Angus MacKinnon

Assessor: Dr Derek K K Lee

Word Count: 9,976

Abstract:

This report details a theoretical investigation of the time-independent, finite temperature, behaviours of Nano-Electro-Mechanical Systems. Based on prior zero-temperature work *[M. Tahir. (2010). Quantum Behaviour in Nano-Mechanical Systems. PhD thesis, ICL.]*. Non-equilibrium Green's function methods were used to model a single site quantum dot in the Coulomb blockage regime, coupled via tunnel junctions to two metallic leads in the wide-band limit. The model was developed to include a quantum harmonic oscillator strongly coupled to the dot. Both electronic and mechanical degrees of freedom were treated quantum mechanically. Finite temperature was incorporated by breaking down the associated Fermi function into a sum over Matsubara poles.

Analytic solutions were found for current through the dot and the density matrix of the dot-oscillator sub-system, recovering prior results in the zero-temperature limit. The system was found to display a mix of quantum and classical behaviour, with step like features resulting from quantisation, whereas the oscillator was driven into a state resembling classical oscillation. The Seebeck effect was found to be significant when the difference of lead thermal energies was comparable to their difference of Fermi energies. Entanglement was shown within the system's density matrix and found to have a strong dependence on coupling strength.

Contents:

Chapter 1:

Introduction to NEMS and the Quantum Limit

1.1 Introduction:

This introduction will provide a discussion of Nano-Electro-Mechanical Systems (NEMS) and the quantum limit, forming the motivation and background for this theoretical project.

Though quantum effects on electronics of sub-micrometre scale are well understood, the same cannot be said about mechanical devices on the same scale. This is due to the increased complexity and sometimes counterintuitive nature of moving parts in the quantum regime, combined with the great difficulty of ultra-precise measurement. Take the simple example of two interlocked gears, the first gear is driven clockwise, the teeth apply force on one another and the second gear turns anticlockwise. However, shrink this system small enough and there is a finite probability the teeth will quantum tunnel through one another. A semi-classical adjustment would be to introduce a 'slipping' rate to account for the tunnelling events. In reality the teeth from the two gears fail to both tunnel and maintain position between each other, causing the gears to enter a mixed quantum state where the teeth can be thought to spend time within each other. This has no classical analogue and must be approached quantum mechanically. [1]

1.1.1 The Quantum Limit:

Where does this transition from classical to quantum occur, and is there a meaningful boundary between the regimes? Or is classical merely a sufficient approximation for bulk quantum behaviour? The most obvious and fundamental limitation on precision is the Heisenberg Uncertainty principle $\Delta x \Delta p \geq \hbar/2$, where Δx is uncertainty in position, Δp is uncertainty in momentum, and $\hbar$ is the reduced plank constant. Applied to the case of a simple harmonic oscillator this gives the zero-point displacement uncertainty or 'Standard Quantum Limit' $\Delta x_{SQL} = \sqrt{\hbar/2m\omega_0}$, with m the effective mass and ω_0 the natural frequency, referring to the uncertainty in position of the oscillator's ground state. A comparison can be draw to the limit $\hbar\omega_0 \geq k_B T$, a regime where the energy of the flexural fundamental mode is greater than the random kinetic energy of particles, the zero-point behaviour of a system becomes significant in this limit. Current dilution refrigeration can routinely achieve temperatures of 30mK, requiring a fundamental

frequency greater than 600MHz for the oscillator. This limit is key to studies of NEMS and to experimental verification of this project. [2][3]

1.1.2 Electro-Mechanical Systems (EMS):

Electro-Mechanical Systems can be simplified to a mechanical element which will deflect and/or vibrate in response to a force. Coupled to an electronic 'transducer' element which converts a change in mechanical energy to an electronic or optical signal. Often in practise an input transducer is used to maintain oscillation of the mechanical element in a known mode and an output transducer used to measure perturbations of the oscillation. The study of EMS on the micrometre scales (MEMS) became established in the mid 1980's and represents an amalgamation of technologies from both semiconductor processing and mechanical engineering. In the present day, the relative ease of mass producing robust micrometre motors and sensors at low cost has been instrumental in fuelling the data dominated age we currently live in. Yet not until the mid 1990's did the experimental study of nanometre scale EMS really begin and we are only now beginning to see practical applications. [4]

1.2 Nano-Electro-Mechanical System (NEMS):

Classical models for mechanical and electronic systems break down at the nanometre scale due to quantum effects. Though difficult to manufacture NEMS are set to revolutionise molecular scale measurement, allowing fast decoding of DNA, and could form an integral part of quantum computers [5]. High 'Q' or quality factors of modern mechanical oscillators, dissipating very little energy and suppressing thermomechanical fluctuations, provide extreme sensitivities to outside damping. NEMS devices can be created that require three to four orders of magnitude less power than their electronic counterparts. Even the first high frequency mechanical resonator built in 1994[4] had a Q factor 100 times that of a typical electronic one. Sensitivities to mass have been pushed down to the attogram scale ($10^{-18}g$) and NEMS could one day be sensitive to the mass of single nucleon, allowing distinction between different molecular isotopes [6]. It seems due to their high sensitivities NEMS are the key to investigating the quantum limit and there are currently several groups perusing this area of research. Mechanical systems scale well to investigate the quantum limit as they vibrate with the approximate angular frequency $\omega_0 = (m/k)^{-1/2}$, where m is the effective mass and k is the effective spring constant. Reducing the size of a system's linear dimension l, will alter mass proportional to l^3, and spring constant proportional to l. Giving ω_0 proportional to $1/l$, hence reducing the size of a mechanical system brings it closer to the quantum limit. [4]

1.2.1 'Doubly Clamped Beam' and Cantilever:

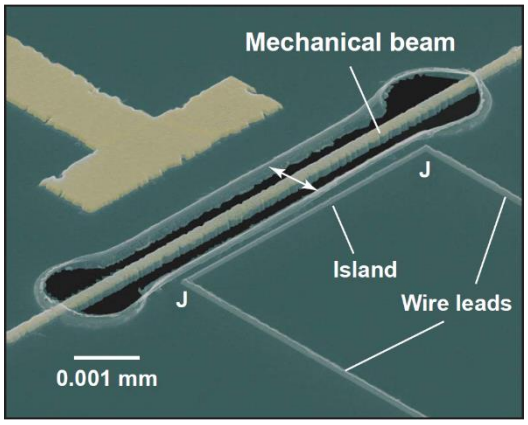

Figure 1.1[8], electron micrograph of a suspended mechanical beam with gate electrode to the top left and SET bottom right. Tunnelling junctions labelled J.

Perhaps the simplest nano-mechanical resonators are the 'doubly clamped beam' (fixed both ends, figure 1.1) and cantilever (fixed one end). Tiny objects often fabricated from silicon onto integrated circuits using techniques from nano-lithography and micro-machining. This has the advantage of allowing electronics to be fabricated onto the mechanical elements, negating orientation difficulties on the sub-micron scale. These beams are large by quantum standards having masses roughly 10^{12} that of a hydrogen atom, but when cooled to millikelvin temperatures to freeze out their flexural modes, act as damped harmonic quantum oscillators. In 1996 A.N. Cleland and M.L. Roukes demonstrated one of the first micron-scale mechanical resonator, a single silicon crystal beam 7.7μm long and 0.33μm by 0.8μm wide, with a measured fundamental frequency of 70.72MHz [7]. More recently in 2004 LaHaye *et al.* demonstrated a similar experiment with more sophisticated electronics, achieving a frequency of roughly 20MHz and temperature of 56mK. Though this beam would have required ~1mK for its zero-point displacement to overcome thermal Brownian motion. Recent experiments using smaller beams to achieve frequencies in the GHz range could in theory allow observation of zero-point motion. The difficulty then becomes measurement of minute displacements, as a 20MHz beam will have a zero-point displacement of 10^{-4}Å, or a thousandth the diameter of a single hydrogen atom [8]. [4][6]

1.2.2 Single Electron Transistor (SET):

Standard micro transducers cannot resolve sub-micron distances, and reducing their size is not viable, as electronic components will suffer from quantum effects and optical from the diffraction limit [4]. A solution is a 'single electron transistor' (SET), modulated by a 'gate' voltage either on a separate electrode or the beam itself. The SET is comprised of an island between two tunnel junctions, small enough that electrons can be considered to quantum tunnel across one by one, driven by a voltage bias. As the beam oscillates it modulates the gate voltage causing modulation of current through the SET, which is amplified and measured. Figure 1.1 shows a separate gate electrode while figure 1.2 show a simplified SET circuit and a mechanical beam doubling as a gate electrode. [2][6]

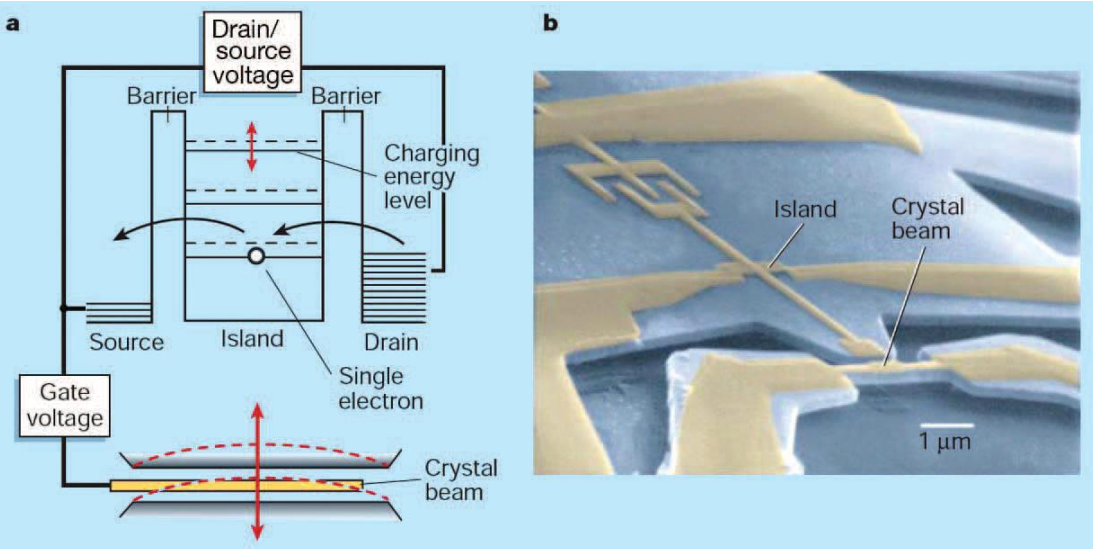

Figure 1.2[6], (*a*) simplified diagram of SET operation. (*b*) False colour SEM micrograph showing suspended beam and SET system, where the beam itself acts as the gate electrode.

The SET is "to date the most promising scheme for achieving quantum zero-point motion sensitivities"[3], yet there are still behaviours obscuring the quantum limit. 'Shot noise' is where the tunnelling electrons dissipate energy into the system as heat, increasing the beam's Brownian motion. Raising gate voltage increases the sensitivity of the SET, though conversely the strength of quantum mechanical coupling between the mechanical and electronic degrees of freedom is also increased. The effect of this is known as 'back action' and can overcome position sensitivity of at high gate voltages. Therefore, to measure the zero-point motion gate voltage must be carefully calibrated and a balance achieved. Nevertheless, back action is an interesting behaviour in and of itself, as it involves a resonator made from tens of billions of atoms, macroscopic in quantum terms, becoming entangled with electrons in the SET. This is another focus of NEMS studies and was first observed by Keith Swab in 2004[6]. [2][3]

More precise implementations of SETs utilise coupling capacitors for increased spatial separation from the oscillator, decreasing the thermal effects of shot noise[2]. For studies of macroscopic quantum superposition states a 'Cooper-pair box' (CPB) is used, consisting of a small superconducting island weakly linked through a tunnel junction to a superconducting electron reservoir. As electrons travel in pairs through superconducting objects there will be a number of pairs on the island at any given time. This CBP is then electrostatically coupled to a mechanical resonator, driving it into a state dependent on the pair state of the box. This can be used to drive the resonator into a superposition of position states, with a potentially observable distinct displacement. Alternatively, after a set 'wait time' the degree of entanglement can be imprinted on the state of the box (figure

3). This is important to investigations of decoherence in mechanical resonators due to their environment. [3][5]

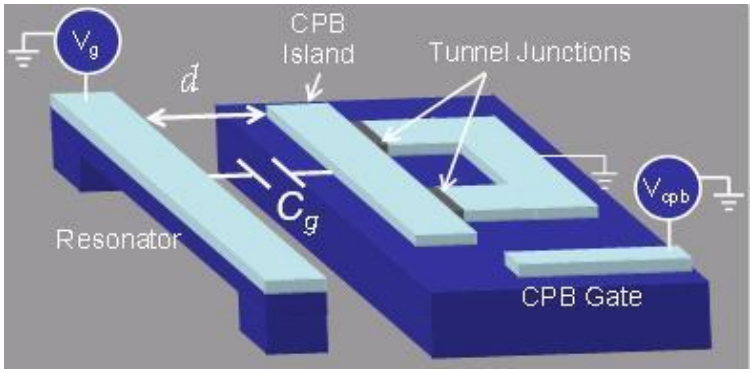

Figure 1.3 [14], showing a Cooper-pair box (centre) and associated superconducting reservoir (right), doubly clamped beam (left) and gate electrodes (bottom right).

1.2.3 Quantum Shuttle:

Quantum shuttles are similar to SETs where electrons tunnel from one contact to another via an island, only in the quantum shuttle case the island oscillates from near one contact to another. As tunnelling rate has an exponential dependence on the physical size of the barrier even slight changes in the shuttle's displacement are significant. Initially proposed by Gorelik *et al.* in 1996[9][10]. Systems coupling a shuttle's vibrational degrees of freedom to electronic ones are a focus of current investigation. The first single-molecule transistor was fabricated by Park *et al.* in 2000 using a C_{60} molecule, showing sharp current increases wherever the bias voltage was high enough to excite vibrational modes[11]. Two separate tunnelling processes occur in these systems. Firstly, incoherent tunnelling where the electron tunnels on and of the dot as separate actions, requiring a phonon for both. Secondly, by 'co-tunnelling' where the electron coherently tunnels without spending significant time on the shuttle, requiring only one phonon and therefore less dependent on dissipative effects. [1][10][12]

1.3 Current Standing and Concluding Remarks:

Though only taking off in the late 90's NEMS remain a fascinating area of study from both a theoretical and practical perspective. The quantum limit was reportedly reached in 2010 by Andrew Cleland *et al.* using a 6GHz mechanical resonator at 25mK[13]. NEMS have come a long way since the rough-cut silicon bridges of the 1990's and although not yet seeing major commercial applications, research has begun branching out. Especially into areas such as quantum computing and biomechanics. More fundamental studies are also continuing, probing the quantum limit and developing even more sensitive displacement and mass detection schemes [14], requiring further development of associated theoretical models such as this piece.

Chapter 2:

Initial Mathematical Formalism

2.1 Introduction:

This chapter will cover the mathematical formalisms used in the project, focussing on using time-independent Green's functions (GF) to analyse the dynamics of a quantum dot between two metallic leads, forming a theoretical model for a SET. The dot is modelled as a single electronic state in the coulomb blockade regime[9], where a second electron with opposite spin cannot occupying the dot, due to coulomb repulsion from the first. While the leads are modelled as semi-infinite in the wide-band approximation and cause a perturbative 'self-energy' effect on the dot. A general discussion of the time-independent single particle GF will be followed by the retarded and advanced GFs along with the characteristic self-energy of the system. These, along with Langreth's theorem and the standard Dyson's equation, will be used to give expressions for the density matrix of the dot and electronic current flowing into the dot. [15][16][17][18][19][20][21][22][23]

2.2 Single Particle Green's Function:

The quantum regime is almost always defined in terms of the Schrödinger equation and associated Hamiltonian operator. A simple time-independent single particle equation can be defined:

$$H\psi = E_s\psi \tag{2.1}$$

Where H is the Hamiltonian operator and ψ the wave function of the system with corresponding energy E_s, however many body systems are described by Hamiltonians which cannot be solved exactly. These systems require the treatment of many body effects as perturbations upon exactly solvable Hamiltonians, here canonical quantisation and Green's functions (GF) become necessary techniques. Assuming ψ can be written as a linear combination of H eigenstates from an orthonormal complete set, the corresponding GF can be defined:

$$[E - H]G(E) = 1 \tag{2.2}$$

Where the Green's function $G(E)$ is subject to the same boundary conditions as the wave function ψ. To get the time-independent formulation of the GF it is assumed the system is coupled together at $t = -\infty$ giving enough time for the system at time $t' = 0$ to not be effected by the initial coupling, giving only dependence on time differences $(t' - t'')$

within the GF. This form can then be Fourier transformed into energy space, giving a time independent form. A formal solution may be written:

$$G(E) = [E - H]^{-1} \tag{2.3}$$

Which is defined everywhere except the singularity $E = E_s$, which is avoided by adding an infinitesimal imaginary part to E.

2.3 Perturbation of Green's Functions:

Defined above is the unperturbed time-independent GF, for the modelled system the perturbed version of this GF is required. Starting again with a Hamiltonian:

$$H = H_0 + \Delta H \tag{2.4}$$

Where H_0 is the original unperturbed Hamiltonian and ΔH the perturbation. H is the new Hamiltonian solved for, from which the perturbed GF $G(E)$ is defined, as in (2.3) with the new H, and the unperturbed GF:

$$g(E) = [E - H_0]^{-1} \tag{2.5}$$

Using this equation, along with (2.4), (2.2) can be rewritten for the perturbed GF in terms of $g(E)$ and ΔH:

$$[E - H_0 - \Delta H]G(E) = 1 \tag{2.6}$$

$$G(E) = [E - H_0]^{-1}\big(1 + \Delta H G(E)\big) \tag{2.7}$$

$$G(E) = g(E) + g(E)\Delta H G(E) \tag{2.8}$$

This is the standard perturbed single particle Dyson's equation.

2.4 Coupled Dot-Leads Model:

In this chapter the modelled system is a single state quantum dot, with a lead on the left (L) and right (R). In the tight binding representation, the Hamiltonian for this system can be written as:

$$H = H_{dot} + H_{leads} + H_{dot-leads} \tag{2.9}$$

Where H_{dot} and H_{leads} are the unperturbed Hamiltonian, representing the uncoupled dot and leads respectively. Then $H_{dot-leads}$is the perturbative term representing the coupling between dot and leads. Defining these terms individually:

$$H_{dot} = \epsilon_0 c_0^\dagger c_0 \tag{2.10}$$

Where ϵ_0 is the energy of the single dot level, and $c_0^\dagger$, c_0 respectively are the creation and annihilation operators for electrons on the dot.

$$H_{leads} = \sum_{j,\alpha} \epsilon_{j,\alpha} c_{j,\alpha}^{\dagger} c_{j,\alpha} \tag{2.11}$$

Where $\alpha = L, R$ is the index for the two leads, j labels the channels in lead α, $\epsilon_{j,\alpha}$ is the energy of channel j, and $c_{j,\alpha}^{\dagger}$, $c_{j,\alpha}$ are the associated creation and annihilation operators for that lead and channel.

$$H_{dot-leads} = \frac{1}{\sqrt{N}} \sum_{j,\alpha} V_{0,\alpha} (c_{j,\alpha}^{\dagger} c_0 + c_0^{\dagger} c_{j,\alpha}) = \Delta H_{0,L} + \Delta H_{0,R} \tag{2.12}$$

Where N is the total number of states in the lead, $V_{0,\alpha}$ represents a coupling factor between the dot and the end state of lead α, and the creation/annihilation operators are as previously defined.

Dyson's equation (2.8) can be rewritten for the dot including the interaction with the leads as:

$$G_{0,0}(E) = g_{0,0}(E) + \sum_{\alpha} g_{0,0}(E) \Delta H_{0,\alpha} G_{\alpha,0}(E) \tag{2.13}$$

Where the 0,0 index refers to the dot, the $0, \alpha$ and $\alpha, 0$ indices refer to dot-lead coupling terms, and α, α to lead specific terms. Note g terms are still unperturbed and G perturbed. Using the Dyson's equation for $G_{\alpha,0}(E)$:

$$G_{\alpha,0}(E) = g_{\alpha,0}(E) + g_{\alpha,\alpha}(E) \Delta H_{\alpha,0} G_{0,0}(E) \tag{2.14}$$

Noting that $g_{\alpha,0}(E) = 0$ as for the unperturbed system there is no coupling. (2.13) can be rewritten as:

$$G_{0,0}(E) = g_{0,0}(E) + \sum_{\alpha} g_{0,0}(E) \Delta H_{0,\alpha} g_{\alpha,\alpha}(E) \Delta H_{\alpha,0} G_{0,0}(E) \tag{2.15}$$

Here it is useful to define the self-energy as:

$$\Sigma_{0,0} = \sum_{\alpha} \Delta H_{0,\alpha} g_{\alpha,\alpha}(E) \Delta H_{\alpha,0} \tag{2.16}$$

This self-energy will be calculated in the next section, for now it can be used to simplify (2.13):

$$G_{0,0}(E) = g_{0,0}(E) + g_{0,0}(E) \Sigma_{0,0} G_{0,0}(E) \tag{2.17}$$

The 0,0 index will now be dropped, unless specified otherwise by alternate double indices all G, g and Σ are for the dot.

2.5 The Self-Energy:

The self-energy represents a perturbative contribution to the dot energy, due to coupling with the leads. Using the wide-band approximation where the contributions to self-energy are considered energy independent, and the electronic density of states can be taken as uniform. The contribution to the self-energy from lead α can be calculated as follows:

$$\Sigma_\alpha = \Delta H_{0,\alpha} g_{\alpha,\alpha}(E) \Delta H_{\alpha,0} \tag{2.18}$$

Where $\mathrm{g}_{\alpha,\alpha}(E)$ the uncoupled GF for the leads is:

$$\mathrm{g}_{\alpha,\alpha}(E) = \frac{1}{N}\sum_j g_{\alpha,j}(E) \tag{2.19}$$

$$= \frac{1}{N}\int_{-\infty}^{+\infty} N \frac{n_\alpha d\varepsilon_\alpha}{E - \varepsilon_\alpha}$$

Where the wide-band approximation has been used to expand $g_{\alpha,j}(E)$, and convert the sum over j into an integral over ε_α, the energy states within lead α. Where n_α is the density of electronic states and N the total number of states in lead α. This integral can be performed with the infinitesimal imaginary factor in E, as a contour around the pole $E = \varepsilon_\alpha$, to give:

$$\mathrm{g}_{\alpha,\alpha}(E) = -i\pi n_\alpha \tag{2.20}$$

As $\mathrm{g}_{\alpha,\alpha}(E)$ is scalar, the resulting equation for Σ_α can be simplified further using the canonical commutation relations of the creation and annihilation operators in ΔH $(=H_{dot-leads})$:

$$\Sigma_\alpha = -i\pi n_\alpha \Delta H_{0,\alpha} \Delta H_{\alpha,0} \tag{2.21}$$

$$= -i\pi n_\alpha \left|V_{0,\alpha}\right|^2$$

$$= -i\Gamma_\alpha/2$$

Where $\Gamma_\alpha = 2\pi n_\alpha \left|V_{0,\alpha}\right|^2$ corresponding to a widening of the dot state, and is inversely proportional to the time an electron spends on the dot. This is the simplified form of the self-energy contribution from lead α, this will vary slightly for different GFs and will be defined where necessary.

2.6 Retarded and Advanced Green's Functions

The retarded GF is non-zero for times $t > t'$, and is used to calculate the response of a system at time t after an earlier perturbation at time t'. While the advanced GF is non-zero for times $t < t'$. For the time-independent case this implies a small positive imaginary factor in E for the retarded GF, and a negative one for the advanced. The Dyson's equation (2.15) can then be rewritten for the retarded (r) and advanced (a) cases:

$$G^{r(a)}(E) = g^{r(a)}(E) + g^{r(a)}(E)\Sigma^{r(a)}G^{r(a)}(E) \tag{2.22}$$

Dropping the 0,0 index as mentioned previously. Where $\Sigma^{r(a)}$ is the retarded (r) or advanced (a) self-energy $\Sigma^{r(a)} = \Sigma_L^{r(a)} + \Sigma_R^{r(a)}$, taking into account contributions from both leads. It is important here to note:

$$\Sigma_\alpha^r = -i\Gamma_\alpha/2 = (\Sigma_\alpha^a)^* \tag{2.23}$$

Defining the advanced and retarded self-energies for lead α.

With the help of (2.5) the equation (2.22) can be rewritten in terms of energy variables:

$$G^{r(a)}(E) = \frac{g^{r(a)}(E)}{1 - g^{r(a)}(E)\Sigma^{r(a)}} \tag{2.24}$$

$$G^{r(a)}(E) = \left[E - E_0 - \Sigma^{r(a)}\right]^{-1} \tag{2.25}$$

These $G^{r(a)}(E)$ functions have poles in one half-plane, retarded in the negative and advanced in the positive. As seen in (2.25) the self-energy term acts as an additional contribution to the dot energy. These functions contain information about the spectral properties and density of states of the system, along with 'lesser' GFs and self-energies they are used calculate physical responses of the system.

2.7 Langreth's Theorem:

In time-dependent studies non-equilibrium GFs are represented as time contours such as the Keldysh contour[15][23]. Though in the time independent case Langreth's theorem can still be applied to give greater and lesser functions. Starting with the spectral function a general expression for lesser function A, pertaining to fermions, in terms of its associated retarded (r) and advanced (a) functions is[22]:

$$A^< = f(\varepsilon)(A^a - A^r) \tag{2.26}$$

Where $f(\varepsilon)$ is the Fermi-Dirac distribution.

Using this equation (2.26) it is simple to show[12] if $A = BC$:

$$A^< = B^r C^< + B^< C^a \tag{2.27}$$

Similarly, if $A = BCD$ it can be shown:

$$A^< = B^r C^r D^< + B^r C^< D^a + B^< C^a D^a \tag{2.28}$$

2.8 The Lesser Green's Function and Self-Energy:

The lesser GF, also called the particle propagator, is more directly linked to physical properties of the system such as particle densities and currents[23]. Using (2.26) the lesser GF can be written:

$$G^<(E) = f(\varepsilon)(G^a(E) - G^r(E)) \tag{2.29}$$

Noting all G's are for the dot, and $f(\varepsilon)$ is the sum of fermi functions for both leads. Then substituting in for $G^a(E)$ and $G^r(E)$ from the Dyson's equation in (2.22) gives:

$$G^<(E) = f(\varepsilon)[g^r(E) + g^r(E)\Sigma^r G^r(E) - g^a(E) - g^a(E)\Sigma^a G^a(E)] \tag{2.30}$$

Using the lesser function equation (2.26) for the single $g(E)$ terms and $g(E)\Sigma\mathrm{G}(E)$ terms separately, then using the Langreth relation in (2.28) for the lesser function resulting from the two $g(E)\Sigma\mathrm{G}(E)$ terms gives:

$$G^<(E) = g^<(E) + g^r(E)\Sigma^r G^<(E) + g^r(E)\Sigma^< G^a(E) + g^<(E)\Sigma^a G^a(E) \tag{2.31}$$

For the unperturbed system $g^<(E)$ can be taken to zero, as the dot is assumed initially empty. Using the relations $1 + \Sigma^{r(a)} G^{r(a)}(E) = \left[1 - g^{r(a)}(E)\Sigma^{r(a)}\right]^{-1}$ and (2.24), (2.31) above can be rewritten:

$$G^<(E) = G^r(E)\Sigma^< G^a(E) \tag{2.32}$$

Which is equivalent to the Keldysh form of the non-equilibrium GF. This result is important because it is directly related to the density by:

$$\rho = -i \int \frac{dE}{2\pi} G^<(E) \tag{2.33}$$

Where ρ is the density matrix for the dot, whose trace gives electron density on the dot, or dot occupation probability as it is a single site. In this simple case without the oscillator ρ will be a single value, whereas with the oscillator ρ will the density matrix of the dot-oscillator system. Taking the trace removes information about the oscillator states as they are normalised, allowing the electronic state to be extracted. The lesser self-energy for lead α can be written using (2.26) as:

$$\Sigma_\alpha^< = f_\alpha(\varepsilon)[\Sigma_\alpha^a - \Sigma_\alpha^r] \tag{2.34}$$

$$= i\Gamma_\alpha f_\alpha(\varepsilon)$$

Where $f_\alpha(\varepsilon)$ is the Fermi function for lead α. The general lesser self-energy is:

$$\Sigma^< = \Sigma_L^< + \Sigma_R^< \tag{2.35}$$

Note that ε is electronic energy of the system, and is related to E the total energy by subtracting out any mechanical energy terms. $\Sigma^<$ will depend explicitly on ε, while $G^{r(a)}$ terms only have explicit E dependence, and $G^<$ terms depend explicitly on E and ε. To avoid potential confusion, the E dependence will be dropped from G's in further equations, though all GF and $\Sigma^<$ terms still have energy dependence.

2.9 Current from Lead α:

I_α the electron current from lead α into the dot is given by the expectation value of the current operator acting for the dot-lead α system[16][17][18][19][20][21]. This can be written as the trace of the current operator acting on the system's density matrix:

$$I_\alpha = Tr(\rho \widehat{I_\alpha}) \tag{2.36}$$

Where $\widehat{I_\alpha}$ is the current operator for lead α into the dot, and ρ is the density matrix of the system. The particle current operator can be defined as:

$$\widehat{I_\alpha} = \frac{ie}{\hbar}\sum_i \left[V_{0,\alpha}c_0^\dagger c_{\alpha,j} - c_{\alpha,j}^\dagger c_0 V_{\alpha,0}\right] \tag{2.37}$$

Where the electron current form of $\widehat{I_\alpha}$ is used, instead of conventional positive charge. This current was used throughout the project as results will be interpreted in terms of electrons flowing on and off the dot. This current operator can then be used in equation (2.36) along with the lesser GF form of the density matrix in (2.33) to rewrite I_α as:

$$I_\alpha = \frac{e}{\hbar}\int \frac{dE}{2\pi}\left[G_{0,\alpha}^< V_{\alpha,0} - V_{0,\alpha}G_{\alpha,0}^<\right] \tag{2.38}$$

Where $G^<$ are dot-lead terms. For this simple no oscillator case GFs are single terms, however with the the oscillator I_α is the trace of the matrix formed on the right of (2.38). Using the Dyson equation for $G_{\alpha,0}$ in (2.14) along with the Langreth relation in (2.27) $A^< = B^r C^< + B^< C^a$, then making use of $g_{\alpha,0}$ and $g_{0,\alpha}$ terms being zero due to no coupling in the unperturbed system, the lesser GF terms in (2.38) above can be written:

$$G_{0,\alpha}^< = G_{0,0}^r V_{0,\alpha} g_{\alpha,\alpha}^< + G_{0,0}^< V_{0,\alpha} g_{\alpha,\alpha}^a \tag{2.39}$$

And

$$G_{\alpha,0}^< = g_{\alpha,\alpha}^r V_{\alpha,0} G_{0,0}^< + g_{\alpha,\alpha}^< V_{\alpha,0} G_{0,0}^a \tag{2.40}$$

Substituting these equations into the current equation (2.38), and making use of $\Sigma_{0,0,\alpha}^{r(a)(<)} = V_{0,\alpha} g_{\alpha,\alpha}^{r(a)(<)}(E) V_{\alpha,0}$ from (2.18) gives:

$$I_\alpha = \frac{e}{\hbar}\int \frac{dE}{2\pi}\left[G_{0,0}^r \Sigma_{0,0,\alpha}^< + G_{0,0}^< \Sigma_{0,0,\alpha}^a - \Sigma_{0,0,\alpha}^r G_{0,0}^< - \Sigma_{0,0,\alpha}^< G_{0,0}^a\right] \tag{2.41}$$

Where the 0,0, α index on the self-energy terms represents the contribution from lead α to the dot term 0,0. Note the GFs have no lead dependence and contain both left (L) and

right (R) self-energy terms, whilst self-energy terms outside GFs are dependent on the α index of I_α. This can be rearranged and the 0,0 index dropped, as an equation with all dot terms has been recovered, to give:

$$I_\alpha = \frac{e}{\hbar}\int \frac{dE}{2\pi}[\Sigma_\alpha^<(G^r - G^a) + (\Sigma_\alpha^a - \Sigma_\alpha^r)G^<] \tag{2.42}$$

This is the general electron current equation that was used throughout the project, for the no oscillator case terms are single values, while for the oscillator they are matrices and current will be the trace. As a convention throughout the report $I = I_L - I_R$ will be used as current through the whole dot-lead system. This equation (2.42) signals then end of the GF mathematical formalism used as the basis of this project.

Chapter 3:

Methodology and Analytic Results

This section will cover development of the specific mathematical model for the systems investigated. Beginning with development of the current equation and density matrix for the no oscillator case discussed in chapter 2, forming a theoretical model of a SET device. Including finite temperature effects that necessitate the fermi function be broken down into a sum over Matsubara frequencies. Not necessary in Muhammad Tahir's thesis, the initial basis of this project, as all temperatures were assumed to be zero.

After formulating this simple case, the system will be expanded to incorporate a quantum harmonic oscillator (QHO) strongly coupled to the dot. This QHO forms the theoretical equivalent of the mechanical element in a physical NEMS, forming a full theoretical realisation of a NEMS device when combined with the dot and leads. The introduction of the QHO changes GF and self-energy terms to matrices indexed by QHO phonon states, it also requires introduction of scattering matrices, mixing the phonon states upon tunnelling events.

3.1 No Oscillator Model:

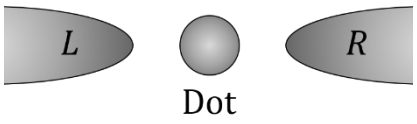

Figure 3.1, Showing the no oscillator system setup. A quantum dot between two metallic leads L and R.

For this simple case, shown in figure 3.1, the form of current equation (2.42) is single valued. As current through the system $I = I_L - I_R$ is being calculated, it is simpler to combine $\Sigma_\alpha^<$ and $G^<$ terms from each lead separately, expand, simplify, and then rearrange before performing the integral. For the $\Sigma_\alpha^<$ terms from each lead in (2.42):

$$(\Sigma_L^< - \Sigma_R^<)(G^r - G^a) = i[\Gamma_L f_L(\varepsilon) - \Gamma_R f_R(\varepsilon)]\left(\frac{1}{E - E_0 + i\Gamma} - \frac{1}{E - E_0 - i\Gamma}\right) \tag{3.1}$$

$$= \frac{2\Gamma}{(E - E_0)^2 + \Gamma^2}[\Gamma_L f_L(\varepsilon) - \Gamma_R f_R(\varepsilon)]$$

Where (2.23) and (2.34) have been used for the self-energies, then (2.25) for the GFs. Note $\Gamma = \frac{1}{2}(\Gamma_L + \Gamma_R)$ the contribution to self-energy from both leads. Similarly combining the $G^<$ terms and using the equation (2.32) for $G^<$ gives:

$$[(\Sigma_L^a - \Sigma_L^r) - (\Sigma_R^a - \Sigma_R^r)]G^< = \tag{3.2}$$

$$= [i\Gamma_L - i\Gamma_R]\frac{1}{E - E_0 + i\Gamma}\left(i\Gamma_L f_L(\varepsilon) + i\Gamma_R f_R(\varepsilon)\right)\frac{1}{E - E_0 - i\Gamma}$$

$$= \frac{\Gamma_R - \Gamma_L}{(E - E_0)^2 + \Gamma^2}[\Gamma_L f_L(\varepsilon) + \Gamma_R f_R(\varepsilon)]$$

Then Combining (3.1) and (3.2) above within the current equation (2.42) gives:

$$I = \frac{e}{\hbar}\int \frac{dE}{2\pi}\frac{2\Gamma_L\Gamma_R}{(E - E_0)^2 + \Gamma^2}[f_L(\varepsilon) - f_R(\varepsilon)] \tag{3.3}$$

Note that this equation is symmetric in terms of gamma contributions from each lead, as changing Γ_L will have the same effect as changing Γ_R, setting $\Gamma_L = \Gamma_R$ recovers a form consistent with the symmetric lead case where the $G^<$ terms cancel in I. This symmetry is justification for assuming the symmetric Γ case, though this could become significant in more complicated models, such as work by M. Ridley (2017)[23]. To perform the integral in (3.3) the Fermi functions must first be broken down into a sum over Matsubara frequencies, for the Fermi function of lead α[24]:

$$f_\alpha(\varepsilon) = \left[\exp\left(\frac{\varepsilon - E_{f\alpha}}{kT_\alpha}\right) + 1\right]^{-1} = \frac{1}{2} - \sum_{n=-\infty}^{+\infty}\frac{kT_\alpha}{\varepsilon - E_{f\alpha} - i\pi(2n+1)kT_\alpha} \tag{3.4}$$

Where $E_{f\alpha}$ is the Fermi energy and T_α the temperature of lead α. k is the Boltzmann constant and ε the electronic energy of the system. It is then possible to perform the integral in (3.3) over each individual Matsubara pole. The results of which form a converging sum, giving a final equation for current. Once this possibility was established Mathematica was used, for convenience and consistency, to perform the integrals and summations analytically. Performing the integral this way for equation (3.3) gives:

$$I = \frac{ie\Gamma_L\Gamma_R}{\pi\hbar(\Gamma_L + \Gamma_R)} \tag{3.5}$$

$$\times\left(\begin{array}{l}\psi\left[\frac{1}{2} + \frac{\Gamma_L + \Gamma_R + 2i(E_0 - E_{fL})}{4\pi kT_L}\right] - \psi\left[\frac{1}{2} + \frac{\Gamma_L + \Gamma_R - 2i(E_0 - E_{fL})}{4\pi kT_L}\right] \\ -\psi\left[\frac{1}{2} + \frac{\Gamma_L + \Gamma_R - 2i(E_0 - E_{fR})}{4\pi kT_R}\right] + \psi\left[\frac{1}{2} + \frac{\Gamma_L + \Gamma_R + 2i(E_0 - E_{fR})}{4\pi kT_R}\right]\end{array}\right)$$

Where $\psi(\dots)$ is the digamma function[25]. Note that in the symmetric Γ case the leads give separate ψ functions. This can be seen in the initial current equation (2.42) where the $G^<$ terms cancel with symmetric Γ, $G^<$ being concerned with the state of the dot. Additionally, the two sets of ψ terms in (3.5) are of the form $(\psi - \psi^*)$, giving an imaginary result. This cancels with i out front, giving a real result for any set of variables, in line with the requirement of real current as an observable.

The electron density on the dot was calculated from the integral over $G^<$ in (2.33), using the same Mataubara frequency method. Taking the symmetric Γ case gives:

$$\rho = \frac{-i}{4\pi}\left(\begin{array}{c} 2i\pi + \psi\left[\frac{1}{2} + \frac{\Gamma + i(E_0 - E_{fL})}{2\pi k T_L}\right] - \psi\left[\frac{1}{2} + \frac{\Gamma - i(E_0 - E_{fL})}{2\pi k T_L}\right] \\ +\psi\left[\frac{1}{2} + \frac{\Gamma + i(E_0 - E_{fR})}{2\pi k T_R}\right] - \psi\left[\frac{1}{2} + \frac{\Gamma + i(E_0 - E_{fR})}{2\pi k T_R}\right] \end{array}\right) \tag{3.6}$$

Of similar form to the current equation (3.5), ensuring a real result for observable ρ, electron density on the dot. In the symmetric temperature case, taking $E_{fL} = -E_{fR}$ gives $\rho = 1/2$, as the ψ terms cancel. This result represents the electron-hole symmetry of the system, where both are equally likely to be charge carriers.

3.2 Oscillator Model:

3.2.1 Basic Formulation:

The physical setup for this model is the SET component from the previous section 3.1, with the addition of a nano-mechanical oscillator placed in close proximity to the dot, shown in figure 3.2. Having the oscillator electrostatically charged causes strong interplay between the tunnelling electrons and the oscillator's frequency, as the electrons alter the charge state of the dot, turning off/on its electrostatic potential, in turn driving the oscillator. Conversely oscillation frequency should influence the current. This is similar in setup to many experimental realisations of NEMS, of a SET coupled to either a doubly clamped beam or cantilever[2][3][7].

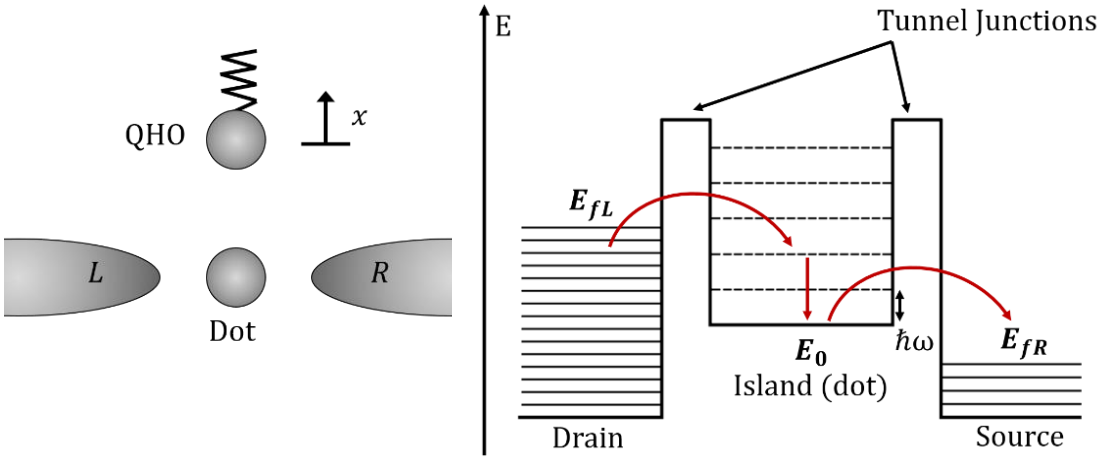

Figure 3.2, showing the oscillator system setup (left), with associated energy level schematic (right). Dotted lines represent phonon creation channels, not states the electron can occupy. The red arrows show an electron's path through the system, tunnelling onto the dot via creation of two phonons.

This theoretical system is considered to be on the nano-scale and in a low temperature regime, such that both electronic and mechanical degrees of freedom can be modelled using previously discussed techniques, and strong coupling can be assumed. The

oscillator is modelled as a QHO, under the assumptions of sufficient damping and low rate of electrons, to give the same initial QHO state for each electron. The addition of the QHO allows electrons to flow through phonon creation and annihilation assisted channels. The Hamiltonian for this system is[12][26][27][28]:

$$H = H_{dot-osc} + H_{leads} + H_{dot-leads} \tag{3.7}$$

Similar to the Hamiltonian for the no QHO system in (2.9), still treating $H_{dot-leads}$ as a perturbation ΔH, but now with a combined term for the dot and oscillator written:

$$H_{dot-osc} = \left[E_0 + \frac{\lambda l}{\sqrt{2}}(b^\dagger + b)\right] c_0^\dagger c_0 + \hbar\omega(b^\dagger b + 1/2) \tag{3.8}$$

Where E_0 is the unperturbed dot energy corresponding to creation and annihilation operators $c_0^\dagger c_0$. $\hbar\omega$ represents the characteristic phonon energy of the QHO, with natural frequency ω, associated with the creation and annihilation operators $b^\dagger b$. λl represents the coupling strength between the oscillator and the dot, and is related to the energy of the capacitor formed by the occupied dot and the charged oscillator given by:

$$eE\hat{x} = \frac{\lambda l}{\sqrt{2}}(b^\dagger + b) \tag{3.9}$$

Where $\lambda = eE$, e the electronic charge on the dot and E its electric field. $l = \sqrt{\hbar/\mu\omega}$ is the zero-point amplitude of the oscillator with mass μ. Here the energy is approximated to have a linear dependence on the displacement of the oscillator x from its equilibrium position. Note that H_{leads} and $H_{dot-leads}$ are still defined as in (2.12) and (2.13) respectively, the same as for the no oscillator case.

3.2.2 Green's Function Formulation:

Similar to the no oscillator case, the dot-lead coupling is treated as a perturbation, while other terms form the H_0 unperturbed system. However, there are additional terms in H_0 and functions are now formed of matrices, where the individual entries $A_{n_0,n}$ denote the initial oscillator state n_0 and final state n. This is not to be confused with the dropped index from chapter 2, written in full these entries would be $A_{0,n_0;0,n}$ with the 0's denoting this matrix is for the dot-oscillator and not the leads, however the 0's have been dropped as all terms are for the dot-oscillator system only.

Given this the self-energies can be calculated similarly to chapter 2; as the QHO does not affect the unperturbed GF for the leads, and the perturbation described by ΔH does not involve any oscillator terms. For the retarded and advanced self-energies $\mathrm{g}_{\alpha,\alpha}^{r(a)}(E - \hbar\omega[n_0 + 1/2])$ must be used instead of $\mathrm{g}_{\alpha,\alpha}^{r(a)}(E)$, as E is still total energy and $\mathrm{g}_{\alpha,\alpha}^{r(a)}$ is concerned with electronic energy. Substituting this and performing the integral in (2.19) the self-energies remains the same for all n_0, giving a diagonal self-energy matrix for lead α, with matrix elements:

$$\Sigma^{r}_{n_0,n_0,\alpha} = (\Sigma^{r}_{n_0,n_0,\alpha})^{*} = \frac{-i\Gamma}{2} \tag{3.10}$$

For the oscillator case symmetric $\Gamma = 2\pi\left|V_{0,L/R}\right|^2 n_\alpha$ is assumed. The lesser self-energy can be calculated similarly, though an extra term encoding the initial temperature state of the oscillator must be added. It is useful for the lesser self-energy to rewrite the integral in (2.19) as:

$$\Sigma^{<}_{n_0,n_0,\alpha} = i\Gamma \int d\varepsilon_\alpha f_\alpha(\varepsilon_\alpha) B_{n_0} \delta(E - \varepsilon_\alpha - (n_0 + 1/2)\hbar\omega) \tag{3.11}$$

$$= i\Gamma f_\alpha(\varepsilon_{n_0}) B_{n_0}$$

Where $\varepsilon_{n_0} = E - (n_0 + 1/2)\hbar\omega$ is the initial electronic energy, ε_α is the energy of lead α, $f_\alpha(\varepsilon)$ is the Fermi distribution function of lead α, and B_{n_0} is the Bose-Einstein factor for state n_0 of the QHO. The lesser self-energy matrix is also diagonal, as the leads are not directly coupled to the oscillator. The initial implementation took the zero-temperature oscillator limit using $B_{n_0} = \delta_{n_0,0}$, where the 0 index refers to the ground state of the oscillator.

Given these self-energy formulations it is possible to calculate the GF terms for the coupled dot-oscillator system. To do this the energy eigenvalues of $H_{dot-osc}$ are required (H_0 for the dot), which can be written:

$$\epsilon = E_0 + (n_0 + 1/2)\hbar\omega - \Delta \tag{3.12}$$

Where ϵ has been used as the energy eigenstate to avoid confusion with E in the GF formalism, E_0 is the unperturbed dot energy, $(n_0 + 1/2)\hbar\omega$ the oscillator energy, and Δ the shift in energy of the QHO potential. Δ does not affect the coupling and was set to zero, in theory Δ could be adjusted experimentally using gate electrodes while maintaining the x shift of the potential. In investigations of this parameter yielded no new features, it can be taken into E_0 without losing physical effects. Given the new energy eigenstates in (3.12) the retarded and advanced GF elements for the dot in (2.25) can be rewritten for the occupied dot phonon representation as:

$$g^{r(a)}_{m,m} = [E - E_0 - (m + 1/2)\hbar\omega \pm i\Gamma]^{-1} \tag{3.13}$$

Where $\Gamma_L = \Gamma_R = \Gamma$ and $\Delta = 0$ have been used. $g^{r(a)}_{m,m}$ is diagonal, and the $+i\Gamma$ is for the retarded (r) and $-i\Gamma$ for the advanced (a). To move to the unoccupied dot representation phonon states a unitary transformation is performed using a scattering or S-matrix represented by $\boldsymbol{\phi}$. The elements $\phi_{n_0,n}$ of the S-matrix give the portion of initial phonon state n_0 in the unoccupied representation transformed to phonon state n in the occupied do representation (with probabilities $\left|\phi_{n_0,n}\right|^2$), calculated in the next section. Using this the GF elements for the unoccupied representation can be written:

$$G^{r(a)}_{n_0,n} = \sum_m \phi_{n_0,m} g^{r(a)}_{m,m} \phi^{\dagger}_{m,n} \tag{3.14}$$

Given the equation for the lesser GF (2.32) holds, the elements of $G^<$ can be written:

$$G^{<}_{n_0,n} = \sum_m G^{r(a)}_{n_0,m} \Sigma^{<}_{m,m} G^{r(a)}_{m,n} \tag{3.15}$$

Where $\Sigma^{<}_{m,m} = \Sigma^{<}_{m,m,L} + \Sigma^{<}_{m,m,R}$ is the contribution from both leads.

3.2.3 S-Matrix ϕ:

The elements of the S-matrix $\phi_{n_0,n}$ were calculated taking the overlap of the QHO energy eigenstate $|n_0\rangle$ in the unoccupied representation with that of $|n\rangle$ in the occupied representation. This QHO eigenstate n_0 can be written in the coordinate basis standard Hermite polynomial form[29]:

$$\Psi_{n_0}(x) = \frac{1}{\sqrt{\sqrt{\pi} 2^{n_0} n_0!\, l}}\, exp\left[-\frac{x^2}{2l^2}\right] H_{n_0}\left({}^{x}/_{l}\right) \tag{3.16}$$

Where $l = \sqrt{\hbar/\mu\omega}$ is the zero-point amplitude of the QHO, x is displacement from the minima of the potential, and $H_{n_0}(\dots)$ is the n_0th Hermite polynomial. To find the eigenstates in the occupied dot representation a linear potential term was added, for the electric field of the occupied dot, altering the QHO potential from $V = \frac{1}{2} m\omega^2 \hat{x}^2$ to:

$$\begin{aligned} V' &= \tfrac{1}{2}\mu\omega^2\hat{x}^2 + \lambda\,\hat{x} \\ &= \tfrac{1}{2}\mu\omega^2(\hat{x} + \lambda/\mu\omega^2)^2 - \lambda^2/2\mu\omega^2 \\ V' &= \tfrac{1}{2}\mu\omega^2(\hat{x} + x_0)^2 - \Delta \end{aligned} \tag{3.17}$$

Where $x_0 = \lambda/\mu\omega^2$ is the x shift and $\Delta = \lambda^2/2\mu\omega^2$ the energy shift of the QHO potential. Δ was set to zero, as the additional potential can include a scalar term to cancel Δ, without altering behaviours. Using this the wave function in (3.16) can be rewritten using the substitution $x \to x + x_0$:

$$\Psi'_n(x) = \frac{1}{\sqrt{\sqrt{\pi} 2^n n!\, l}}\, exp\left(-\frac{(x + x_0)^2}{2l^2}\right) H_n\left(\frac{1}{l}(x + x_0)\right) \tag{3.18}$$

Where Ψ'_n is for the QHO energy eigenstate $|n\rangle$ in the occupied representation. To find $\phi_{n_0,n}$ the overlap of these two wave functions (3.16) and (3.18) was calculated, written in terms of dimensionless $x/l \to x$ and $x_0/l \to x_0$ as:

$$\phi_{n_0,n} = A_{n_0,n} \int exp\left(-\tfrac{1}{2}x^2\right) H_{n_0}(x) exp\left(-\tfrac{1}{2}(x+x_0)^2\right) H_n(x+x_0)dx \qquad (3.19)$$

$$A_{n_0,n} = \frac{1}{\sqrt{\sqrt{\pi}2^{n_0+n}n!\,n_0!}}$$

Making a substitution $y = x + \frac{1}{2}x_0$ and $y_0 = \frac{1}{2}x_0$ gives a form which can be integrated using the standard integral[30]:

$$\int exp(-y^2) H_n(y+y_0) H_{n_0}(y-y_0)dy \qquad (3.20)$$

$$= 2^{n_0}\sqrt{\pi}n!\,(-y_0)^{n_0-n} L_n^{n_0-n}(2{y_0}^2) \qquad \text{For } n_0 \geq n$$

and $$= 2^{n}\sqrt{\pi}n_0!\,(y_0)^{n-n_0} L_{n_0}^{n-n_0}(2{y_0}^2) \qquad \text{For } n_0 \leq n$$

Where $L_q^p(x)$ are the Laguerre Polynomials[31]. These two solutions can be used to write the general form of the overlap matrix elements:

$$\phi_{n_0,n} = \sqrt{\frac{\min[n_0,n]\,!}{\max[n_0,n]\,!\,2^{|n_0-n|}}}\; exp\left(-\frac{{x_0}^2}{4}\right)(\pm x_0)^{|n_0-n|} L_{\min[n_0,n]}^{|n_0-n|}\left(\frac{{x_0}^2}{2}\right) \qquad (3.21)$$

Where $(+x_0)^{|n_0-n|}$ is for $n_0 \leq n$ and $(-x_0)^{|n_0-n|}$ for $n_0 \geq n$. This gives a real unitary matrix for $\boldsymbol{\phi}$ used in further calculations. As a check for analytic errors the elements $\phi_{n_0,n}$ were also calculated using the momentum space wavefunctions. The original wavefunction in (3.16) was Fourier transformed into k-space giving a wave function of form:

$$\Psi_{n_0}(k) = \frac{(-i)^{n_0}}{\sqrt{\sqrt{\pi}2^{n_0}n_0!\,l}}\; exp\left[-\frac{l^2k^2}{2}\right] H_{n_0}(lk) \qquad (3.22)$$

Where $k = p/\hbar$ and p is momentum. The shift of the QHO potential provides a phase shift of $\exp(-ikx_0)$, and the overlap integral was rearranged into the standard form[30]:

$$\int exp(-(x-y)^2) H_n(x) H_{n_0}(x)dx = 2^{n_0}\sqrt{\pi}n!\,(y)^{n_0-n} L_n^{n_0-n}(-2y^2) \qquad (3.23)$$

For $n_0 \geq n$, and with $n_0 \leftrightarrow n$ for $n_0 \leq n$. With $x = lk$ and $y = -\frac{i}{2l}x_0$ before scaling to dimensionless units. Working through this formulation gives an answer in agreement with (3.21). This differs by a factor of $(-i)^{|n_0-n|}$ to M. Tahir (2010)[12], due to choosing the Fourier space wave function equal to the real space one. Taking the Fourier transform

of the real space wave function causes $\Psi_{n_0}(k)$ to differ by $(-i)^{n_0}$. This was chosen to agree with the real space overlap, an overlap of purely real functions that is itself real. Though this discrepancy has no impact on observables, as diagonal elements of current and density matrices are real in both treatments.

3.2.4 Current Equation:

Taking symmetric Γ, it is possible to rewrite the current equation (2.42) for the oscillator case as:

$$I = \frac{e}{\hbar}\sum_{n_0}\int \frac{dE}{2\pi}\left(\Sigma^{<}_{n_0,n_0,L} - \Sigma^{<}_{n_0,n_0,R}\right)\left(G^{r}_{n_0,n_0} - G^{a}_{n_0,n_0}\right) \tag{3.24}$$

Where the diagonal nature of $\mathbf{\Sigma}^{<}_{\alpha}$ has been used. Substituting in for the lesser self-energy from (3.11) and for the GF terms from (3.14) gives:

$$I = \frac{ie\Gamma}{\hbar}\sum_{n_0,n}\left|\phi_{n_0,n}\right|^2 B_{n_0}\int \frac{dE}{2\pi}\left(f_L(\varepsilon_{n_0}) - f_R(\varepsilon_{n_0})\right)\left(g^{r}_{n,n} - g^{a}_{n,n}\right) \tag{3.25}$$

Where $\varepsilon_{n_0} = E - (n_0 + 1/2)\hbar\omega$, and $g^{r(a)}_{n,n} = [E - E_0 - (m + 1/2)\hbar\omega \pm i\Gamma]^{-1}$. In this form, the integral can be evaluated using the same Matsubara technique discussed in the no oscillator case, performing the integral over individual Matsubara terms then summing. This was achieved using Mathematica to get an analytic solution for the current $I = I_L - I_R$:

$$I = \frac{ie\Gamma}{\hbar}\sum_{n_0,n}\left|\phi_{n_0,n}\right|^2 B_{n_0}\begin{pmatrix} \psi\left[\frac{1}{2} + \frac{\Gamma + i\left(E_0 - E_{fL} - (n_0 - n)\hbar\omega\right)}{2\pi kT_L}\right] \\ -\psi\left[\frac{1}{2} + \frac{\Gamma - i\left(E_0 - E_{fL} - (n_0 - n)\hbar\omega\right)}{2\pi kT_L}\right] \\ -\psi\left[\frac{1}{2} + \frac{\Gamma - i\left(E_0 - E_{fR} - (n_0 - n)\hbar\omega\right)}{2\pi kT_R}\right] \\ +\psi\left[\frac{1}{2} + \frac{\Gamma + i(E_0 - E_{fR} - (n_0 - n)\hbar\omega)}{2\pi kT_R}\right] \end{pmatrix} \tag{3.26}$$

Similar to the no oscillator current equation (3.5), with a sum over digamma functions ψ in from $i(\psi - \psi^*)$. Note the $\frac{1}{2}\hbar\omega$ in the Fermi function cancels with the $\frac{1}{2}\hbar\omega$ from the GF, and the current is still in direction of electron flow. This was initially formulated for the simplified case of zero oscillator temperature $B_{n_0} = \delta_{n_0,0}$, which sets the n_0 index in (3.26) above to zero.

3.2.5 Density Matrix:

Using the equations derived in this chapter and the formalisms of chapter 2, the density matrix of the dot-oscillator system was calculated. Using the density equation (2.33) and the $\boldsymbol{G}^{<}$ in (3.15) the element $\rho_{n_0,n}$ of the density matrix $\boldsymbol{\rho}$ can be written:

$$\rho_{n_0,n} = -i \sum_{m} \int \frac{dE}{2\pi} G^{r}_{n_0,m} \Sigma^{<}_{m,m} G^{a}_{m,n} \tag{3.27}$$

Substituting in for the GF from (3.14) and the lesser self-energy from (3.11), noting $\Sigma^{<}_{m,m} = \Sigma^{<}_{m,m,L} + \Sigma^{<}_{m,m,R}$, gives the form:

$$\rho_{n_0,n} = -i \sum_{m,r,a} \int \frac{dE}{2\pi} \phi_{n_0,r} g^{r}_{r,r} \phi^{\dagger}_{r,m} i\Gamma B_m [f_L(\varepsilon_m) + f_R(\varepsilon_m)] \phi_{m,a} g^{a}_{a,a} \phi^{\dagger}_{a,n} \tag{3.28}$$

Where the index r is used for retarded GF terms in the occupied dot representation, and a for the advanced. This integral was performed in Mathematica using the Matsubara technique to give:

$$\rho_{n_0,n} = \frac{\Gamma}{2\pi} \sum_{m,r,a} \frac{\phi_{n_0,r} \phi^{\dagger}_{r,m} \phi_{m,a} \phi^{\dagger}_{a,n} B_m}{[(a-r)\hbar\omega + 2i\Gamma]} \tag{3.29}$$

$$\times \left(\begin{array}{l} 2i\pi + \psi\left[\frac{1}{2} + \frac{\Gamma - i\left(E_0 - E_{fL} - (m-a)\hbar\omega\right)}{2\pi k T_L}\right] \\ -\psi\left[\frac{1}{2} + \frac{\Gamma + i\left(E_0 - E_{fL} - (m-r)\hbar\omega\right)}{2\pi k T_L}\right] \\ +\psi\left[\frac{1}{2} + \frac{\Gamma - i\left(E_0 - E_{fR} - (m-a)\hbar\omega\right)}{2\pi k T_R}\right] \\ -\psi\left[\frac{1}{2} + \frac{\Gamma + i(E_0 - E_{fR} - (m-r)\hbar\omega)}{2\pi k T_R}\right] \end{array} \right)$$

Again, this was initially calculated for $B_{n_0} = \delta_{n_0,0}$. The electron density on the dot is given by the trace of matrix $\boldsymbol{\rho}$, or algebraically $\rho = \sum_n \rho_{n,n}$. Note ρ for the $E_0 = 0$ and $E_{fL} = -E_{fR}$ case is still $1/2$, as the the digamma terms cancel over the indices m, r and a, and the resulting $2i\pi$ term converge to $1/2$ over $\rho_{n,n}$. (3.29) above is the final result of chapter 2, the analytic functions calculated in this chapter were investigated in Mathematica and used to generate graphs; to compare the different cases and influence of variables.

Chapter 4:

Discussion of Results

4.1 Introduction:

This section will cover discussion of the equations derived in the previous section. Graphs generated in Mathematica and figures will be used to compliment this discussion. Beginning with the current equation, with comparisons drawn across the three cases of: no oscillator, zero temperature oscillator, and finite temperature oscillator. Followed by a discussion of asymmetric lead temperature. Then a discussion of the electron density on the dot, which leads into a discussion of the density matrix and potential entanglement of the system.

Errors will be discussed throughout, though graphs were generated in Mathematica using analytic functions, and investigations found no significant numerical errors due to this. However, it is important to note that an approximation was made for the $\boldsymbol{\phi}$ matricies. For the $\boldsymbol{\phi}$ matrices to be unitary ($\boldsymbol{\phi}^{\dagger} = \boldsymbol{\phi}^{-1}$) they must also be infinite, which is not possible computationally. An investigation of this problem found for coupling $x_0 < 1$ the entries $\phi_{n_0,n}$ fall off quickly with increasing n_0 and/or n, and a 5×5 matrix was found to be sufficient approximation for $\boldsymbol{\phi}$. Additionally, $\boldsymbol{\phi}^{-1}$ was used instead of $\boldsymbol{\phi}^{\dagger}$ to maintain normalisation, further reducing numerical errors.

Unless specified otherwise all input variables were scaled to units of $\hbar\omega$, taken to be the natural energy scale of the system. Apart from x_0, the dimensionless ratio of the QHO potential's x shift between representations, to its zero-point displacement.

4.2 Electron Current:

4.2.1 No Oscillator Case:

To view behaviours of the system a graph of E_0, the unperturbed dot energy, against current I gives the necessary features. This corresponds to setting up an experimental system with a constant bias across the leads and only varying the dot energy using a gate voltage. Using equation (3.5) for the no oscillator case a graph of $E_0/\hbar\omega$ against $I/e\omega$ has

been plotted in figure 4.1, with $E_{fL} = 8\hbar\omega$ as the higher Fermi level and $E_{fR} = 3\hbar\omega$ the lower. Positive current indicates flow of electrons from left (L) to right (R).

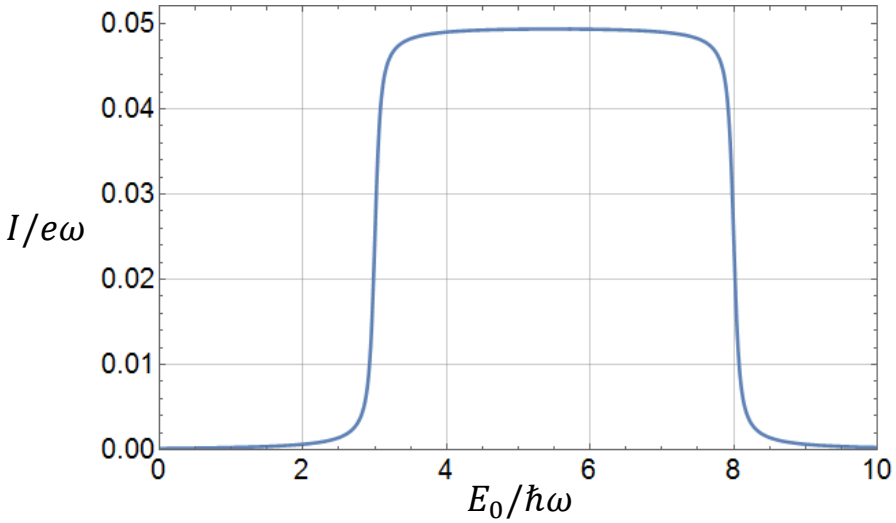

Figure 4.1, Showing current $I/e\omega$ against dot energy $E_0/\hbar\omega$ for the no oscillator case. Using variables: $E_{fL} = 8\hbar\omega$, $E_{fR} = 3\hbar\omega$, $\Gamma = 0.05\hbar\omega$ and $kT = 0.1\hbar\omega$.

Energy must be conserved within the dot-lead system, meaning particles must tunnel from an occupied state to an unoccupied state with equal energy. This is shown by figure 4.1 where for $E_0 < E_{fR}$ (the lower Fermi level) there is zero current, electrons tunnel into the dot from the left lead but cannot tunnel out, due to a lack of unoccupied levels, shown by figure 4.2a. However, for $E_{fR} < E_0 < E_{fL}$ electrons can tunnel in from the left lead and out into the right lead, shown by figure 4.2b, and current is seen to flow in figure 4.1. Then for $E_{fR} < E_{fL} < E_0$ no current flows as the dot energy is higher than both the Fermi levels, and electrons cannot tunnel into it from either lead, shown by figure 4.2c.

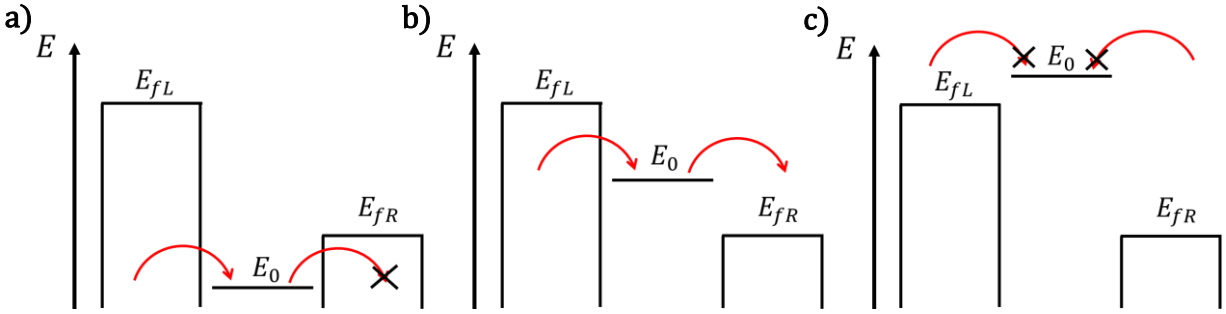

Figure 4.2, simple energy level diagrams of the dot-leads system, all states below the fermi levels are considered occupied and red arrows show an electrons path through the system. 4.2a shows an electron tunnelling onto the dot but not off, due to a lack of unoccupied sites. 4.2b shows electrons flowing through the system from left to right. 4.2c shows a lack of occupied levels with sufficient energy to tunnel onto the dot.

In the zero temperature, low gamma limit the graph in figure 4.1 will tend towards a rectangular function. The smoothing effects seen are cause by Γ broadening the energy of the bound state on the dot, and temperature kT causing a distribution of electron energies

around each leads Fermi energy, providing electrons of energy above and unoccupied states below.

4.2.2 Zero Temperature Oscillator Case:

Using equation (3.26) with the simplification $B_{n_0} = \delta_{n_0,0}$ a graph of E_0 against I is plotted in figure 4.3. For consistency the same Fermi levels, Γ, and kT as the no oscillator case are used. The additional features are due to phonon creation transitions, where electrons in the leads with energy $E = E_0 + n\hbar\omega$ can lose $n\hbar\omega$ to tunnel into the dot, creating n phonons in the oscillator. Phonon annihilation transitions are not seen due to a lack of energy in the initial state of the oscillator.

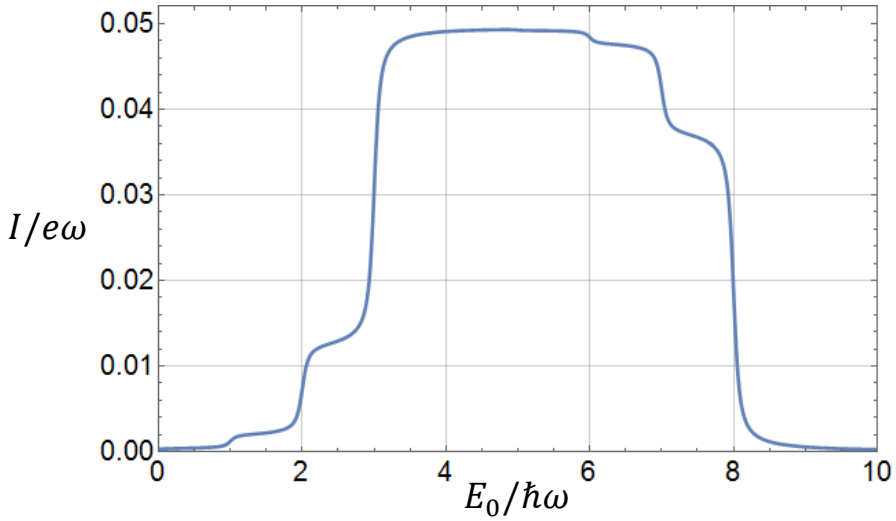

Figure 4.3, Showing current $I/e\omega$ against dot energy $E_0/\hbar\omega$ for the zero-temperature oscillator case. Using variables: $E_{fL} = 8\hbar\omega$, $E_{fR} = 3\hbar\omega$, $\Gamma = 0.05\hbar\omega$, $kT = 0.1\hbar\omega$ and $x_0 = 0.75$.

Figure 4.3 is similar to the no oscillator case, with additional features due to phonon creation. The step like features just below $E_{fL} = 8\hbar\omega$ represent a drop in current as the dot energy E_0 becomes higher than $E_{fL} - n\hbar\omega$ cutting off the transition creating n phonons. Figure 4.4a shows the $n = 1$ transition, which is cut off for $E_0 > 7\hbar\omega$. Note the contributions to the current decay exponentially with increasing n, so much so that the $n = 3$ transition is not clearly visible. Further evidence the 5×5 $\boldsymbol{\phi}$ matrix is an acceptable approximation, as it neglects transitions higher than $n = 5$.

The step like features for E_0 leading up to $E_{fR} = 3\hbar\omega$ were initially unexpected, however an inspection of the formulation found the results to be consistent with previous work[12][23]. Through investigation this result was found to be inconsistent with M. Tahir's (2010)[12] explanation that n phonons are created by the electron on the dot, which leaves with energy $E_0 - n\hbar\omega$. As there are no unoccupied states of energy $E_0 - n\hbar\omega$ for the electron to tunnel into. Furthermore, investigations of the density matrix for these systems show no phonons remaining after the electron has tunnelled out the dot. The features were found to have the same x_0 dependence as the features in 4.4a, showing they

are phonon assisted. Though further investigation of the time-dependent model would be required to determine their exact nature.

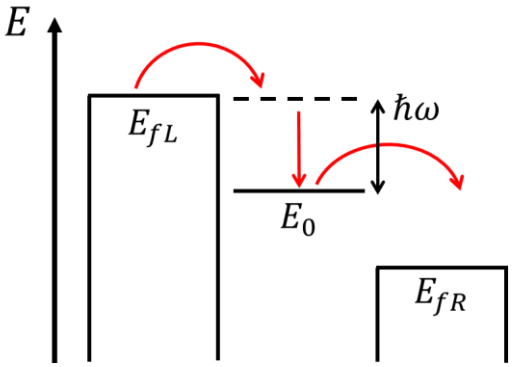

Figure 4.4, a simple energy level diagram of the system, the dotted line represents a conduction channel via creation of a single phonon. The red arrows show an electron utilising this channel to tunnel into the dot, then tunnelling out into the right lead.

4.2.3 Finite Temperature Oscillator Case:

Using current equation (3.26), but with B_{n_0} factors according to the Bose-Einstein distribution for a finite oscillator temperature, a graph of E_0 against I is plotted in figure 4.5. Using the same variable as previous cases. Figure 4.5 is similar to both previous cases, with further smoothing caused by the oscillator temperature, and additional features just above both Fermi levels, $E_{fL} = 8\hbar\omega$ and $E_{fR} = 3\hbar\omega$, due to phonon annihilation events. As the oscillator now has a characteristic temperature it is in a distribution of phonon states, from which energy can be absorbed by electrons, opening up new conduction channels. This case was not investigated by previous zero temperature work.

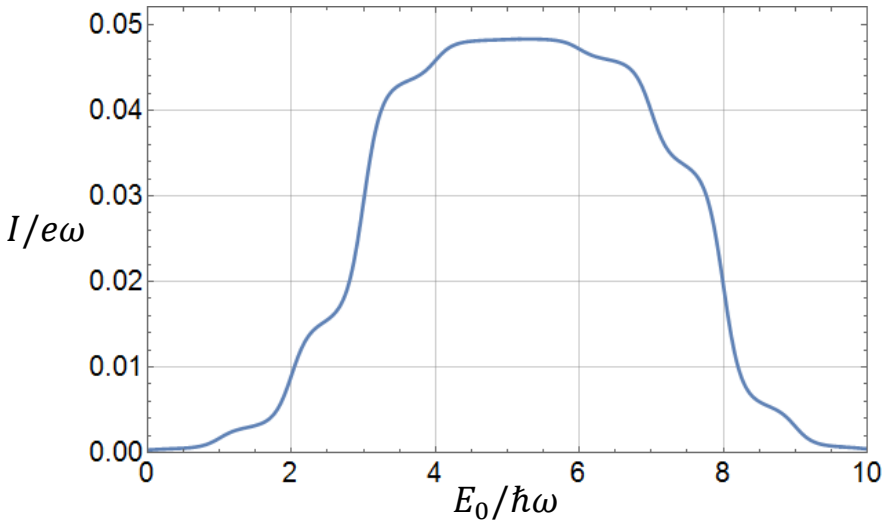

Figure 4.5, showing current $I/e\omega$ against dot energy $E_0/\hbar\omega$ for the finite-temperature oscillator case. Using variables: $E_{fL} = 8\hbar\omega$, $E_{fR} = 3\hbar\omega$, $\Gamma = 0.05\hbar\omega$, $kT_{leads} = 0.1\hbar\omega$, $kT_{oscillator} = 1\hbar\omega$ and $x_0 = 0.75$.

The additional step like feature just above $E_{fL} = 8\hbar\omega$ can be explained by electrons with energy $E_0 - \hbar\omega$ in the left lead absorbing a phonon from the oscillator to tunnel into the dot. This is shown in figure 4.6a, and is cut off when $E_0 > E_{fL} + \hbar\omega$. Conversely the feature just above $E_{fR} = 3\hbar\omega$ is the same effect for the right lead, however in this orientation

electrons flow back out into the right lead, showing in figure 4.6b. This has the effect of blocking electrons from the left lead, which is why an increase in current is seen when this transition is cut off at $E_0 = 4\hbar\omega$. Features are also expected just below both Fermi levels, where electrons on the dot absorb energy from the oscillator to tunnel out, an example of which is in figure 4.6c. Though this is difficult to discern from the graph, due to increased smoothing from the oscillator's temperature, and an investigation of the time-dependent case would be required to break down all possible transitions.

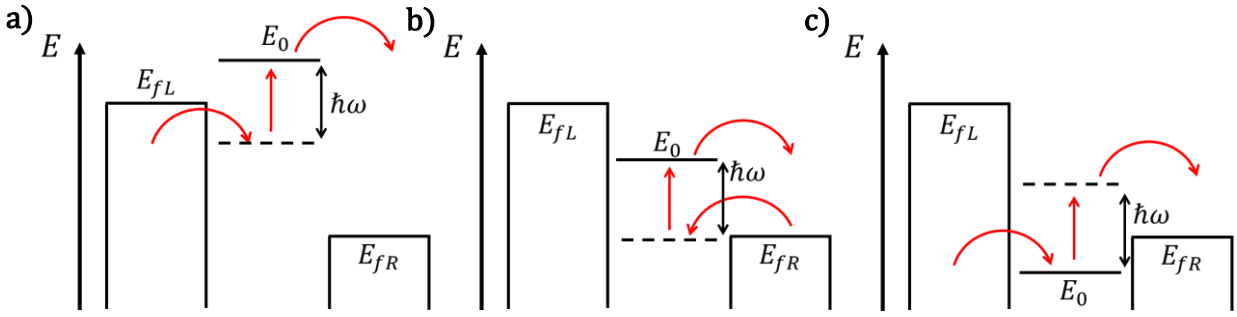

Figure 4.6, energy level diagrams of the dot-leads-QHO system. 4.6a shows an electron tunnelling into the dot via a phonon annihilation channel (dotted line), then tunnelling out again. 4.6b shows tunnelling via phonon annihilation, then back out into the same lead. 4.6c shows tunnelling in, then tunnelling out via phonon annihilation.

To make phonon annihilation features visible the system must be setup with the oscillator temperature much higher than that of the leads, assumed to be at the ambient temperature of the system. Due to the nature of the Bose-Einstein distribution this requires a high ratio of kT to $\hbar\omega$, for significant occupation of the first excited oscillator state. Whereas for phonon assisted features to be visible against background temperature, a low ratio of kT to $\hbar\omega$ is required. This can be avoided by setting the oscillator temperature higher than the leads, in the case of figure 4.4 $kT_{leads} = 0.1\hbar\omega$ whilst $kT_{osc} = 1\hbar\omega$. This disparity and the lack of visible annihilation features for $kT_{leads} = kT_{oscillator} = 0.1\hbar\omega$, justifies focusing on the zero-temperature oscillator case to reduce computation times drastically.

4.2.4 Saturation Current:

Looking at the current graphs, figures 4.1, 4.3 and 4.5, not only do they follow the same general shape, they also give similar maximum current or 'saturation current'. To investigate this analytically E_{fL} was taken to $+\infty$ and E_{fR} to $-\infty$, in this regime $f_L(\varepsilon) = 1$ and $f_R(\varepsilon) = 0$, removing temperature and dot energy dependencies. For the no oscillator case this gives $I = e\Gamma/\hbar$. Γ represents the widening of the dot's bound state and is inversely proportional to the average time between tunnelling events, so this linear dependence is as expected. Supported by the electron density on the dot going to $1/2$ in this regime.

The same treatment can be used for the zero and finite temperature oscillator cases, giving:

$$I = \frac{e\Gamma}{\hbar}\sum_{n_0,n}\left|\phi_{n_0,n}\right|^2 B_{n_0} = \frac{e\Gamma}{\hbar} \tag{4.1}$$

Due to the normalisation of both $\phi_{n_0,n}$ and B_{n_0}. Though the finite temperature oscillator in figure 4.5 has a maximum noticeably below $\Gamma = 0.05\hbar\omega$, due to finite temperature and dot energy effects close to the Fermi levels. It appears the presence of the oscillator interferes with the resonant tunnelling of the no phonon transition, possibly due to 'back action'[6], though the sum of phonon assisted contributions gives the same saturation current.

4.3 Seebeck Effect/ Thermoelectric Power:

As lead temperature has not been assumed symmetric or set to zero in derivations, it is possible to investigate the Seebeck or thermoelectric effect[32]. Where current is produced due to temperature gradients within the system. This was investigated for the no oscillator and zero temperature oscillator cases, using Mathematica to manipulate input variables and plot graphs of their dependencies.

4.3.1 No Oscillator Case:

For the no oscillator case, a temperature gradient across the system when $E_{fL} = E_{fR} = E_0$ gave zero current. Due to the symmetric nature of occupied and unoccupied sites in the Fermi distribution around the Fermi energy, meaning any gain in tunnelling into the dot would be lost due to a gain in tunnelling out. While for the dot energy above both Fermi levels, $E_{fL} = E_{fR} < E_0$, by an amount comparable to the lead's temperature difference ΔkT, a current would be produced flowing from the higher temperature 'hot' lead to the lower temperature 'cold' lead. Due to a greater number of electrons in the hot lead with sufficient energy to tunnel into the dot, and as a secondary factor more unoccupied states in the cold lead for electrons to tunnel out into. For a dot energy below both Fermi levels, $E_{fL} = E_{fR} > E_0$, by $\sim\Delta kT$, current was seen to flow from cold to hot lead. Due to more unoccupied states in the hot lead below its Fermi level for electrons to tunnel into from the dot. This does not violate the second law of thermodynamics, as electrons flow below the Fermi level and will have the effect of heating up the cold lead and cooling the hot.

The Seebeck effect is significant for an applied bias (unequal Fermi levels) when the difference of the two fermi levels ΔE_f is of comparable size to ΔkT. Figure 4.7 shows a graph of current against dot energy where $\Delta E_f = 0.2\hbar\omega$ centred at zero, for both $\Delta kT = 0$ the dashed line, and $\Delta kT = 0.3\hbar\omega$ the solid line. Note as in previous sections $E_{fL} > E_{fR}$. The Seebeck effect can be seen to overpower the applied bias for $E_0 < E_{fR}$, whilst increasing normal flow of current for $E_0 > E_{fL}$. With a liminal phase in between, due to the energy distribution in the hot lead causing less electrons in states around the dot

energy. The zero-current intercept tends to the Fermi level of the cold lead as the temperature of the hot lead tends to infinity.

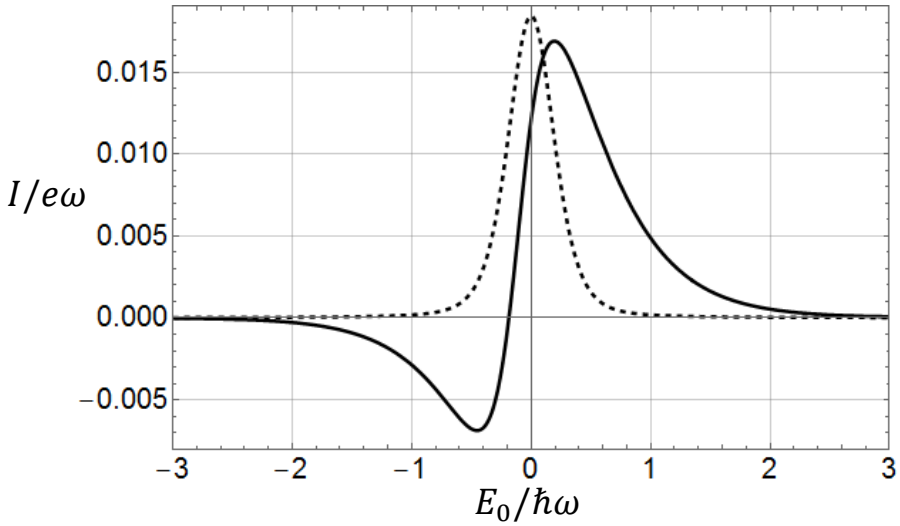

Figure 4.7, showing current $I/e\omega$ against dot energy $E_0/\hbar\omega$ in the no oscillator case, for $\Delta kT = 0$ (dashed line) and $\Delta kT = 0.3\hbar\omega$ (solid line). Using variables: $E_{fL} = 0.1\hbar\omega$, $E_{fR} = -0.1\hbar\omega$, $\Gamma = 0.05\hbar\omega$ and $kT_R = 0.1\hbar\omega$.

4.3.2 Zero Temperature Oscillator Case:

For the oscillator case a temperature gradient does produce a current for $E_{fL} = E_{fR} = E_0$, provided kT for the hot lead is of comparable size to $\hbar\omega$, shown by figure 4.8. Due to the oscillator breaking the symmetry of electron distributions around tunnelling energies (E_0), by providing phonon assisted conduction channels of higher energy. This effect should be reduced in the finite temperature oscillator, which also opens up conduction channels of lower energy.

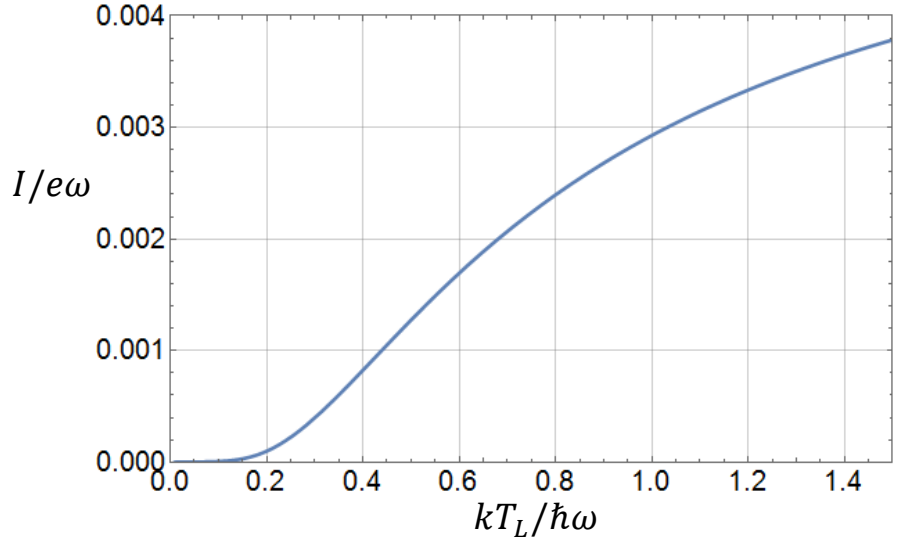

Figure 4.8, showing current $I/e\omega$ against left lead temperature $kT_L/\hbar\omega$ in the oscillator case. Using variables: $E_{fL} = E_{fR} = E_0 = 0$, $\Gamma = 0.05\hbar\omega$, $kT_R = 0.1\hbar\omega$ and $x_0 = 0.75$.

The Seebeck effect is still significant in the zero-temperature oscillator case for an applied bias $\Delta E_f \sim \Delta kT$, as shown in figure 4.9. With the dotted line for $\Delta kT = 0$ and solid line for $\Delta kT = 0.3\hbar\omega$, with $\Delta E_f = 0.2\hbar\omega$. The same cold to hot flow is seen overpowering the bias for $E_0 < E_{fR}$, and increasing current for $E_0 > E_{fL}$. A smaller thermoelectric effect was also found around $E_0 = E_f - n\hbar\omega$, as phonon assisted conduction channels follow the same rules as the no phonon channel. However, this is difficult to see as it is easily overpowered by the no phonon channel or the smoothing effects of temperature, but is significant in a high $\hbar\omega$ low kT_R limit. The finite temperature oscillator case was not taken due to time constraints though may be worth further study, additionally the temperature gradient behaviours when the oscillator is set to a specific energy eigenstate $|n\rangle$ could be investigated.

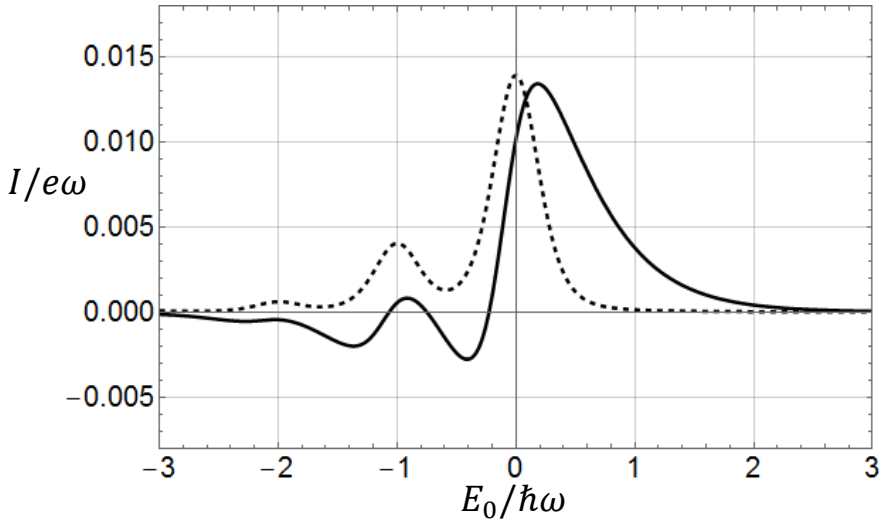

Figure 4.9, showing current $I/e\omega$ against dot energy $E_0/\hbar\omega$ in the oscillator case, for $\Delta kT = 0$ (dashed line) and $\Delta kT = 0.3\hbar\omega$ solid line. Using variables: $E_{fL} = 0.1\hbar\omega$, $E_{fR} = -0.1\hbar\omega$, $\Gamma = 0.05\hbar\omega$, $kT_R = 0.1\hbar\omega$ and $x_0 = 0.75$.

4.4 Electron Density on the Dot:

4.4.1 No Oscillator Case:

Using the density equation (3.6), with the same variables as the current graphs, a graph of electron density on the dot ρ was plotted against dot energy E_0, shown in figure 4.10. This graph substantiates the interpretation of figure 4.1. For $E_0 < E_{fR} = 3\hbar\omega$ density tends to 1, the dot is always occupied, and current is blocked via coulomb blockage. Analogous to no current as electrons cannot tunnel out of the dot. For $E_0 > E_{fL} = 8\hbar\omega$ density drops to zero, as the dot energy is too high for electrons to tunnel in, and zero current flows. As discussed in chapter 3 for symmetric E_{fL} and E_{fR} either side of E_0 ($E_0 = 5.5\hbar\omega$ for figure 4.10), density becomes $1/2$. Representing the electron-hole symmetry of the system, where both particles have equal likelihood of being the charge carriers. Figure 4.10 shows density is approximately $1/2$ for E_0 between both Fermi levels, but not within a few kT or Γ of either. Showing resonant tunnelling happens within a relatively small

window around E_0, controlled by Γ and kT. Combined with figure 4.1 for the current, this suggests current has a dependency on electron-hole symmetry, where the symmetric case has more viable conduction channels and therefore higher total current.

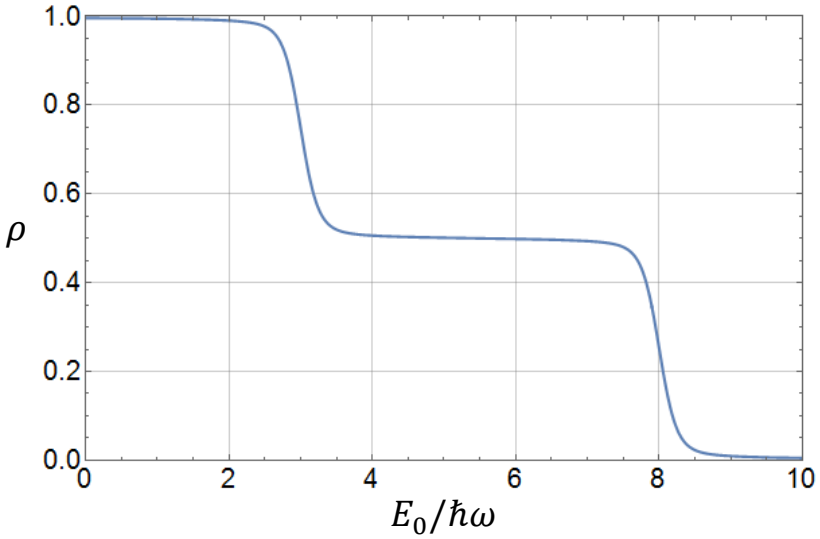

Figure 4.10, Showing electron density on the dot ρ against dot energy $E_0/\hbar\omega$ for the no oscillator case. Using variables: $E_{fL} = 8\hbar\omega$, $E_{fR} = 3\hbar\omega$, $\Gamma = 0.05\hbar\omega$ and $kT = 0.1\hbar\omega$.

4.4.2 Zero Temperature Oscillator Case:

Using (3.29) a graph of ρ against E_0, for the same variables as 4.3, is shown in figure 4.11, where ρ is the trace of the density matrix. The additional features just below each Fermi level are due to the phonon creation assisted channel discussed for the current graphs, figures 4.3 and 4.4. When cut off, the additional channels push the density away from 1/2, associated with a decrease in current. This points towards a breaking of the electron-hole symmetry, where channels for one particle are cut off, although investigation of the time dependent case would be required to investigate this further.

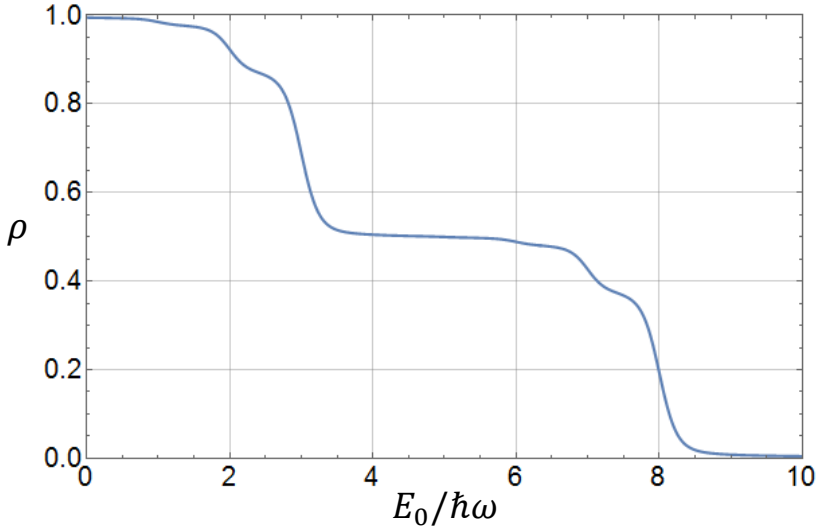

Figure 4.11, Showing density ρ against dot energy $E_0/\hbar\omega$ for the zero-temperature oscillator case. Using variables: $E_{fL} = 8\hbar\omega$, $E_{fR} = 3\hbar\omega$, $\Gamma = 0.05\hbar\omega$, $kT = 0.1\hbar\omega$, and $x_0 = 0.75$.

4.4.3 Finite Temperature Oscillator Case:

Using (3.29) a graph of ρ against E_0, for the same variables as 4.5, is shown in figure 4.12. The additional features are due to the additional phonon annihilation assisted channels discussed for figures 4.5 and 4.6. Again, significant additional smoothing can be seen due to the high oscillator temperature compared to that of the leads.

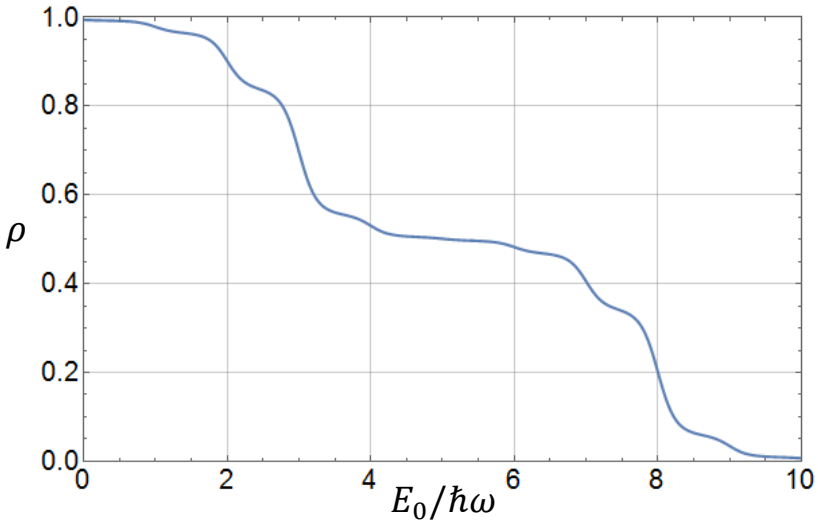

Figure 4.12, Showing density ρ against dot energy $E_0/\hbar\omega$ for the finite-temperature oscillator case. Using variables: $E_{fL} = 8\hbar\omega$, $E_{fR} = 3\hbar\omega$, $\Gamma = 0.05\hbar\omega$, $kT_{leads} = 0.1\hbar\omega$, $kT_{oscillator} = 1\hbar\omega$, and $x_0 = 0.75$.

4.5 Entanglement:

4.5.1 Identifying Entanglement

Given equations (3.29) for $\rho_{n_0,n}$ it is possible to calculate the density matrix of the dot-oscillator system, from which it is possible to determine whether the system is entangled. This extension was not investigated in previous work[12][23]. Entangled states are non-separable, meaning the wave function for the dot and oscillator cannot be written either side of a tensor product:

$$|\psi_{dot-osc}\rangle \neq |\psi_{dot}\rangle \otimes |\psi_{osc}\rangle \tag{4.2}$$

Where $|\psi_{dot-osc}\rangle$ is the wavefunction for the dot-oscillator system, $|\psi_{dot}\rangle$ for only the dot, and $|\psi_{osc}\rangle$ only the oscillator. As $\boldsymbol{\rho} = |\psi\rangle\langle\psi|$ this corresponds to a density matrix that when diagonalised has multiple non-zero entries/eigenvalues. Investigations were limited to the zero-temperature oscillator case. Figure 4.13 below shows such a density matrix for the case of E_0 far below both Fermi levels, in a low gamma regime. For this system, multiple non-zero eigenvalues were found suggesting entanglement.

$$\boldsymbol{\rho} = \begin{pmatrix} 0.62 & 0.24 & 0.06 & 0.01 & 0.00 \\ 0.24 & 0.25 & 0.13 & 0.04 & 0.02 \\ 0.06 & 0.13 & 0.10 & 0.04 & 0.02 \\ 0.01 & 0.04 & 0.05 & 0.02 & 0.02 \\ 0.00 & 0.01 & 0.02 & 0.01 & 0.01 \end{pmatrix} \quad \underline{\lambda} = \begin{pmatrix} 0.75 \\ 0.21 \\ 0.03 \\ 0.00 \\ 0.00 \end{pmatrix}$$

Figure 4.13, Showing density matrix $\boldsymbol{\rho}$ with eigenvectors $\underline{\lambda}$, suggesting entanglement. Using variables: $E_{fL} = E_{fR} = 10\hbar\omega$, $\Gamma = 0.01\hbar\omega$, $kT = 0.1\hbar\omega$, and $x_0 = 0.75$. Values have been approximated to two decimal places for clarity.

Multiple non-zero eigenvalues were found for all orientations of the Fermi and dot energy levels where $E_0 \lesssim E_{f>} - \hbar\omega$, where $E_{f>}$ is the higher of the two Fermi levels. Corresponding to entanglement whenever electrons flow into the dot through multiple conduction channels. Given an oscillator in the first excited state entanglement is found for $E_0 \lesssim E_{f>}$, due a phonon annihilation channel being open. With n additional phonons E_0 can be raised by $n\hbar\omega$, though eigenvalues drop exponentially with required phonon annihilation numbers. It is unclear how physically viable it is to maintaining the oscillator in an excited state, as long-time averages have been assumed. However further investigation of entanglement in the time-dependent and finite-temperature oscillator formulations may prove rewarding.

It was found that each channel adds to an eigenvalue associated with the number of phonons created, e.g. the ground state transition adds to the first eigenvalue and the single phonon creation channel to the second. Suggesting they represent relative transport probability through the associated channel. Eigenvectors then suggest the distribution of end phonon states for the associated conduction channel, due to $\boldsymbol{\phi}$ mixing. The density matrix can also be calculated with the phonons in the occupied dot representation by removing the outer two $\boldsymbol{\phi}$ matrices in equation (3.28). This gives the same eigenvalues as the unoccupied representation, but a more diagonal density matrix, as each switching between representations mixes the phonon states.

Additional investigation of $\boldsymbol{\rho}$ and it's eigensystem suggest while eigenvalues refer to specific phonon transitions, the end oscillator state is a mix of phonon states given by diagonal elements of $\boldsymbol{\rho}$. Allowing a characteristic final temperature for the oscillator to be calculated from diagonal elements of $\boldsymbol{\rho}$. A temperature associated with the no phonon transition was found, suggesting 'shot noise' was a factor, caused by the $\boldsymbol{\phi}$ matrix's mixing effect. This process also suggests the oscillator is driven into a mixed phonon state, with a non-zero displacement expectation value, which in the time-dependent cause would look like classical oscillation back and forth in the potential.

4.5.2 Measuring Entanglement:

Given the system is entangled, it should be possible to measure the degree of entanglement. A standard measure for this is the Shannon entropy[33]:

$$S(\boldsymbol{\rho}) = -Tr(\boldsymbol{\rho}\log_2\boldsymbol{\rho}) = -\sum_i \lambda_i \log_2 \lambda_i \tag{4.3}$$

Where $S(\boldsymbol{\rho})$ is the Shannon entropy and λ_i are the eigenvalues of $\boldsymbol{\rho}$. This measure requires the trace of the density matrix be 1, this is not the case for most orientations modelled, specifically any where current can flow. This is due to lead terms missing from $\boldsymbol{\rho}$. However, for E_0 far below both Fermi levels the trace (electron density) is 1, and it is possible to calculate $S(\boldsymbol{\rho})$. Figure 4.14 shows a plot of $S(\boldsymbol{\rho})$ against x_0 the coupling strength, for three cases of $\boldsymbol{\phi}$ matrix size: the dashed line for a 2×2 matrix, solid line for 5×5, and dot-dashed for 10×10. This shows entanglement increases with coupling x_0 and tends to zero when x_0 does, as expected. This graph shows the 5×5 $\boldsymbol{\phi}$ matrix at $x_0 = 0.75$, used for analysis throughout this project, is a sufficient approximation for the infinite $\boldsymbol{\phi}$ matrix, as there is little to no divergence from the 10×10 matrix. Nevertheless, for higher x_0 the values diverge due to numerical errors, and a larger matrix must be used.

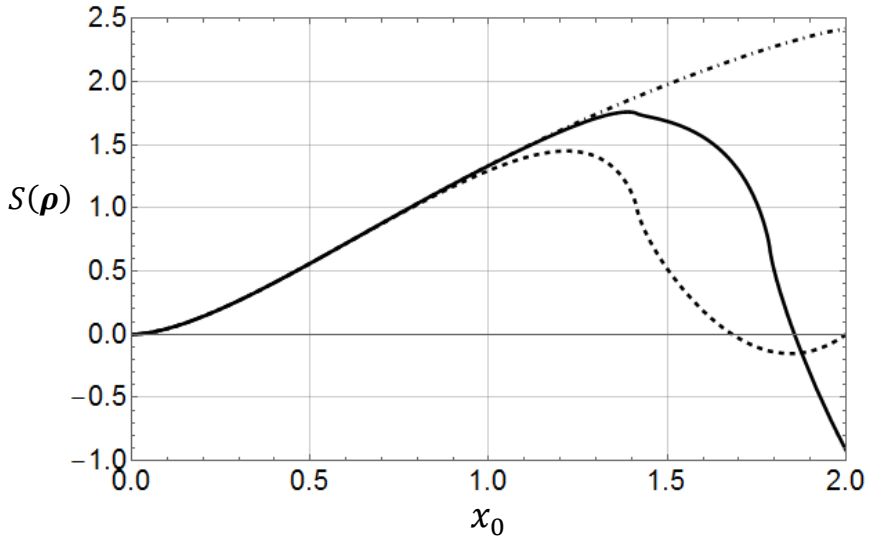

Figure 4.14, Showing Shannon entropy $S(\boldsymbol{\rho})$ against coupling strength x_0. Using variables: $E_{fL} = E_{fR} = 100\hbar\omega$, $E_0 = 0$, $\Gamma = 0.01\hbar\omega$, $kT = 0.1\hbar\omega$. For $\boldsymbol{\phi}$ matrix: 2×2 dashed line, 5×5 solid line and 10×10 dot-dashed line.

Chapter 5:

Concluding Remarks

Finite temperature was successfully incorporated into the zero temperature work this project was based upon[12], with the zero temperature results recovered when temperature is taken to zero. Temperature generally had a smoothing effect on plotted graphs, due to distribution of electron energies around Fermi levels; though finite temperature within the oscillator caused additional behaviours.

Given temperature was incorporated the Seebeck effect could be investigated, an extension of previous work. This effect was found to be significant in the $\Delta E_f \sim \Delta kT$ regime, with electron flow possible both from cold to hot and vice versa. This could be developed further to investigate the effects of oscillator temperature and time-dependent factors.

Previous work was also extended by investigating entanglement within the system's density matrix. However, this was limited due to an incomplete density matrix, and the long-time averaged nature of the time-independent case. It would be an interesting avenue of further study to investigate the time-dependent case, incorporating both leads into the density matrix.

The system was shown to exhibit behaviour associated with both quantum and classical behaviour. Entanglement is inherently quantum and the step like features are key indicators of energy quantisation. Whereas the final states of the oscillator seem classical with their associated non-zero displacement expectation values.

Current NEMS systems can achieve natural frequencies of order 1GHz[13][34], this corresponds to roughly 1mK temperatures for the required ratios in this project. This is an order of magnitude greater than the temperatures produced using dilution refrigeration[3][4]. Nevertheless, with fabrication techniques becoming increasingly refined, these theoretical results may soon be verified experimentally.

6. Acknowledgements:

I would like to thank my supervisor Professor Angus MacKinnon for his excellent supervision, without which none of this would have been possible. I would also like to thank my project partner for his assistance throughout, and Professor Ulrik Egede for quick and concise replies to my formatting questions. Finally thank you to my family for their support and for providing the best possible environment for writing this report.

7. Bibliography:

[1] A Mackinnon. (2005). Theory of some nano-electro-mechanical systems. Physica E. 29, 399-410.

[2] M. D. LaHaye, O. Buu, B. Camarota, K. C. Schwab. (2004). Approaching the Quantum Limit of a Nanomechanical Resonator. Science. 304, 74-77.

[3] M. Blencowe. (2004). Quantum electromechanical systems. Physics Reports. 395, 159-222.

[4] M. Roukes. (2001). Nanoelectromechanical systems face the future. Physics World. 25-31.

[5] A. Cho. (2003). Researchers Race to Put the Quantum Into Mechanics. Science. 299, 36-37.

[6] M. P. Blencowe. (2005). Nanoelectromechanical systems. Contemporary Physics. 46 (No.4), 249-264.

[7] A. N. Clelanda and M. L. Roukes. (1996). Fabrication of high frequency nanometer scale mechanical resonators from bulk Si crystals. Applied Physics Letters. 69, 2653-2655.

[8] M. Blencowe. (2004). Nanomechanical Quantum Limits. Science. 304, 56-57.

[9] L.Y. Gorelik, A. Isacsson, M.V. Voinova, R. Kaesmo, R.I. Shekhter and M. Jonson. (1998). Shuttle Mechanism for Charge Transfer in Coulomb Blockade Nanostructures. Physics Review Letters. 80, 4526-4529

[10] A.D. Armour and A. MacKinnon. (2002). Transport via a quantum shuttle. Physical Review B. 66, 1-10.

[11] H. Park, J. Park, A. K. L. Lim, E. H. Anderson, A. P. Alivisatos & P. L. McEuen. (2000). Nano-mechanical oscillations in a single-C60 transistor. Nature. 407, 57-59.

[12] M. Tahir. (2010). Quantum Behaviour in Nano-Mechanical Systems. PhD thesis, Imperial College London.

[13] P. Rodgers. (2010). Nanomechanics: Welcome to the quantum ground state. Nature Nanotechnology. 5, 245.

[14] Roukes Group. Current Research Efforts. Available: http://nano.caltech.edu/research/index.html. Last accessed 29th Apr 2017.

[15] L.V. Keldysh. (1965). Diagram Technique for Nonequilibrium Processes. Journal of Experimental and Theoretical Physics. 20 (4), 1018.

[16] S Datta. (1990). A simple kinetic equation for steady-state quantum transport. Journal of Physics: Condensed Matter. 2 (40), 8023-8052.

[17] R. Lake, S. Datta. (1992). Nonequilibrium Green's-function method applied to double-barrier resonant-tunneling diodes. Phys. Rev. B. 45 (12), 6670.

[18] R. Lake, S. Datta. (1992). Energy balance and heat exchange in mesoscopic systems. Phys. Rev. B. 46 (8), 4757-4763.
[19] Y. Meir and N. S. Wingreen. (1992). Landauer formula for the current through an interacting electron region. Phys. Rev. Lett.. 68 (16), 2512.
[20] N. S. Wingreen, A.-P. Jauho, and Y. Meir. (1993). Time-dependent transport through a mesoscopic structure. Phys. Rev. B. 48 (11), 8487.
[21] A.-P. Jauho, N. S. Wingreen, and Y. Meir. (1994). Time-dependent transport in interacting and noninteracting resonant-tunneling systems. Phys. Rev. B. 50 (8), 5528.
[22] H. Huag, A.-P. Jauho. (1998). Quantum Kinetics in Transport and Optics of Semi-conductors. Berlin: Springer-Verlag. 35-55.
[23] M. Ridley. (2017). Time-Dependent Quantum Transport and Fluctuations in Molecular Junctions. PhD thesis, Imperial College London.
[24] T. Matsubara. (1995). A New Approach to Quantum-Statistical Mechanics. Progress in Theoretical Physics. 14 (4), 351–378.
[25] Weisstein, Eric W. "Digamma Function." From MathWorld--A Wolfram Web Resource. Accesible: http://mathworld.wolfram.com/DigammaFunction.html. Last accessed 29th Apr 2017.
[26] M. Galperin, A. Nitzan, M. A. Ratner. (2006). Resonant inelastic tunneling in molecular junctions. Phys. Rev. B. 73 (4), 045314.
[27] M. Tahir and A. MacKinnon. (2008). Quantum transport in a resonant tunnel junction coupled to a nanomechanical oscillator. Phys. Rev. B. 77 (22), 224305.
[28] . Aji, J.E. Moore, C.M. Varma. (2003). Electronic-vibrational coupling in single-molecule devices. arXiv:cond-mat/0302222v2 [cond-mat.mes-hall]. (2).
[29] D. J. Griffiths (2004). Introduction to Quantum Mechanics. 2nd ed. New Jersey: Prentice Hall. 31-43.
[30] I.S. Gradshteyn, I.M. Ryzhik (1980). Table of Integrals, Series and Products, Corrected and Enlarged Edition. London: Academic Press. 36-37.
[31] I.S. Gradshteyn, I.M. Ryzhik (1980). able of Integrals, Series and Products, Corrected and Enlarged Edition. London: Academic Press. 1037.
[32] F. J. DiSalvo. (1999). Thermoelectric Cooling and Power Generation. Science. 285 (5428), 703-706.
[33] N. J. Cerf and R. Cleve. (1997). Information-theoretic interpretation of quantum error-correcting codes. Phys. Rev. A. 56 (3), 1721-1732.
[34] A. Gaidarzhy, M. Imboden, P. Mohantya, J. Rankin, B. W. Sheldon. (2007). High quality factor gigahertz frequencies in nanomechanical diamond resonators . Applied Physics Letters . 91 (20), 203503.